Geophysical Journal International

Surface wave mode coupling and the validity of the path average approximation in surface waveform inversions: an empirical assessment

Arjun Datta,[1] Keith F. Priestley,[1] Steve Roecker[2] and Chris H. Chapman[3]

[1]*Bullard Laboratories, Department of Earth Sciences, University of Cambridge, Madingley Road, Cambridge CB3 0EZ, United Kingdom.*
E-mail: arjundatta23@gmail.com
[2]*Rensselaer Polytechnic Institute, Troy, NY 12180, USA*
[3]*Schlumberger Gould Research, High Cross, Madingley Road, Cambridge CB3 0EL, United Kingdom*

SUMMARY

We employ an empirical approach to study the phenomenon of surface wave mode conversion due to lateral heterogeneity, and, as an example, assess its impact on a specific waveform inversion methodology used for surface wave tomography. Finite difference modelling in 2-D media, using a method that allows modelling of a single surface wave mode at a time, is combined with frequency domain decomposition of the wavefield onto a basis of local mode eigenfunctions, to illuminate mode conversion as a function of frequency and heterogeneity parameters. Synthetic waveforms generated by the modelling are inverted to study the effects of mode conversion on the inversion process. For heterogeneities in the upper mantle depth range of ∼40–300 km, we find that heterogeneity strengths of about 5 per cent (with sharp lateral boundaries), or lateral boundary length scales of 10–15 times the seismic wavelength (with 10 per cent maximum strength) produce significant mode conversion at periods of 30 s and shorter. These are significant in the sense that, depending on source strength, converted mode amplitudes can be well above typical noise levels in seismology. Correspondingly, waveform inversion with higher modes reveals the inadequacy of the path average approximation at these periods, with the potential for errors as large as 7 per cent in inferred group velocities, which will translate into errors in the inverted shear-velocity structure.

Key words: Numerical modelling; Waveform inversion; Seismic tomography; Surface waves and free oscillations; Wave propagation.

1 INTRODUCTION

Global tomographic models of the mantle (e.g. Debayle & Ricard 2012; Priestley & McKenzie 2013; Schaeffer & Lebedev 2013; French & Romanowicz 2014; Moulik & Ekström 2014) are now fairly consistent in terms of large-scale isotropic shear velocity structure, with differences between models being most pronounced for small-scale features and at greater depths. Since surface waves are an integral part of the V_s tomography toolkit, it is clear that the next generation of global V_s models will come from incorporating higher frequency surface waves and higher mode numbers than are typically used today. Until fully numerical solutions of the forward problem become the norm, the challenge in going to higher frequencies and higher modes is largely theoretical, that is, it lies in maintaining the accuracy of the forward solution, whilst keeping the inverse problem tractable.

Ray theory for surface waves has played a dominant role in surface wave tomography, whether in its simple linearized form commonly recognized as the great-circle path (GCP) approximation (Woodhouse & Dziewonski 1984) or the more accurate full ray theory also referred to as the WKBJ approximation (Woodhouse 1974; Babich et al. 1976; Yomogida 1985; Tromp & Dahlen 1992a,b). There are two limitations of ray theory. First, it is an infinite frequency approximation that cannot account for the finite zone of sensitivity of travelling waves and second, it is only valid for smoothly varying media where length scales of variations are much larger than the seismic wavelength. The former has led to much debate in the general seismological community (e.g. Montelli et al. 2004; Van Der Hilst & De Hoop 2005) and for surface waves, it has been shown that finite frequency effects can be accounted for by proper regularization of ray-theory based inversions, provided that path coverage is sufficiently dense (Sieminski et al. 2004; Levshin et al. 2005; Trampert & Spetzler 2006). Moreover, finite frequency effects are less important as we tend towards higher frequencies. The second limitation, with implications for along-path heterogeneity in Earth structure, has also been studied extensively, at least in

terms of assessing the validity of the GCP approximation (Lay & Kanamori 1985; Woodhouse & Wong 1986; Pollitz 1994; Wang *et al.* 1998; Ritzwoller *et al.* 2002). Within the realm of along-path effects, there is another, less understood issue not accounted for by ray theory—that of interactions or coupling between surface wave modes. Unlike the aforementioned effects, mode coupling is exacerbated with higher frequencies (Meier *et al.* 1997) and higher modes, so it is worth studying on its own.

Most surface wave tomography relies on first extracting dispersion information from the observed surface waveforms by comparing them with waveforms commonly synthesized by the summation of modes computed in a laterally homogeneous reference model. In such a model, the individual modes propagate independently; however, in more realistic heterogeneous Earth models, surface wave propagation can be more complex. Dispersion can still be extracted from the observed waveforms by comparing them with synthetic waveforms computed for a laterally homogeneous reference model by modal summation, but in this case, the modes are coupled by the lateral heterogeneity (Maupin 2007). This represents a computational issue necessitated by an inability to compute the modes of more complicated Earth models, and is distinct from mode interference (e.g. Thatcher & Brune 1969). Mode interference can exist in a homogeneous or heterogeneous Earth model, but the mode coupling we describe is present only in a heterogeneous Earth model. In this paper, we focus on mode coupling—in the sense of mode conversion of local modes (see Maupin 2007)—but are aware that mode interference is another issue with multi-mode surface wave analysis.

The theory describing mode coupling was first developed, in 2-D, by Kennett (1984). The theory was later extended to 3-D (Tromp 1994; Kennett 1998), but never found mainstream use in large-scale data analysis or inversions due to prohibitive computational requirements. On the other hand, in the realm of body wave modelling by mode summation, the importance of mode coupling whether using normal modes (Li & Tanimoto 1993; Li & Romanowicz 1995) or surface wave modes (Marquering & Snieder 1995; Marquering *et al.* 1996) is widely acknowledged and methods accounting for mode coupling have been extensively used (Li & Romanowicz 1996; Marquering & Snieder 1996; Zhao & Jordan 1998; Mégnin & Romanowicz 2000; Gung *et al.* 2003; Panning & Romanowicz 2006; Lekić & Romanowicz 2011; French *et al.* 2013; French & Romanowicz 2014). Just as body wave phases modelled by mode summation have unrealistic, laterally homogeneous sensitivity kernels if mode coupling is ignored, so too for surface waves, the presence of along-path heterogeneity renders phase sensitivity kernels laterally heterogeneous (see Maupin 2007)—an effect which cannot be described by WKBJ theory. Yet the importance of mode coupling for exclusive modelling of surface waves (discounting those studies, as in references above, where surface waves are a subset of the data used) has received much less attention and it continues to be neglected in the popular multimode surface wave tomography techniques in existence today (e.g. Cara & Lévêque 1987; Nolet 1990; Gee & Jordan 1992; van Heijst & Woodhouse 1997; Ekström *et al.* 1997). The individual waveform inversions that underlie these techniques are based on forward modelling that cannot account for mode coupling, hence the path average approximation implicit in them is valid only in so far as mode conversions (if any) do not corrupt the measurements made on the data to extract different modes. As a case study we investigate the Cara & Lévêque (1987, hereafter CL1987) waveform inversion method.

Zhou *et al.* (2004) used sensitivity kernels for surface wave observables to conclude that mode coupling was negligible at the typical resolution scales of global surface wave tomography. However their analysis was restricted to the fundamental mode only. In this paper we take a very simple, empirical approach towards quantifying mode coupling and gaining a practical understanding of when the path average approximation is rendered invalid by it. In particular, we examine synthetic seismograms generated by finite difference (FD) forward modelling in 2-D media with varying degrees of lateral heterogeneity. Restricting the study to 2-D models ensures that other wave propagation effects (off-path scattering etc.) are eliminated so that mode conversion can be studied unambiguously. Mode coupling is studied in the simplest sense of conversion among local modes.

2 MODELLING AND ANALYSIS METHODS

2.1 Finite difference modelling

Synthetic seismograms in 2-D media are computed using a hybrid algorithm that combines the 2.5-D FD approach to solving the wave equation described in Roecker *et al.* (2010) with the source specification of Bielak *et al.* (2003) as implemented by Baker & Roecker (2014). We adopted this algorithm because it was relatively easy to adapt the code to the objectives of this study. Adapting the Bielak *et al.* (2003) approach implies specifying the source only at the boundary and computing the total field within the heterogeneous medium, as opposed to computing only a scattered field (with sources internal to the medium) which was the approach of Roecker *et al.* (2010). Fortunately, the former can be easily adapted from the Baker & Roecker (2014) implementation without sacrificing any of the multimode capabilities of the latter.

This modified technique still requires the specification of a background wavefield in the region outside the model, and to do so we use the method of Gomberg & Masters (1988) to compute the response of a 1-D medium to a seismic excitation. This method uses a propagator matrix technique to solve the eigenproblem for surface wave dispersion, combined with the Mendiguren (1977) description of surface wave radiation, to obtain Green's functions for a specified moment-tensor source. The 2.5-D FD algorithm is a frequency-domain approach; time-domain seismograms are generated after convolving the total field with a Gaussian source time function.

As our study is a new application of this algorithm, we subjected it to a battery of tests to ensure that the results would be sufficiently accurate for the analysis presented here. A detailed review of these tests appears in Appendix A, and as a general conclusion we found that the numerical errors were acceptably small. One result worth noting involved the combination of a rotated grid and mass lumping adapted by Roecker *et al.* (2010) from the work of Jo *et al.* (1996) and Štekl & Pratt (1998), to reduce the density of grid points required to mitigate numerical anisotropy and dispersion. We found that their optimized weighting of masses and grids, while adequate for short distances (<1000 km), does not sufficiently reduce dispersion at distances we seek to model in this study (see Fig. A2). While it may be possible to re-evaluate their optimal coefficients for denser grid spacing (their study was geared towards 4 grid points per minimum wavelength) our tests showed that we could achieve an acceptably small level of numerical error by weighting the rotated grids more or less equally (the actual weights are 0.6 and 0.4) and increasing the grid density to 12 points per minimum wavelength while, somewhat surprisingly, lumping only the four 'nearest
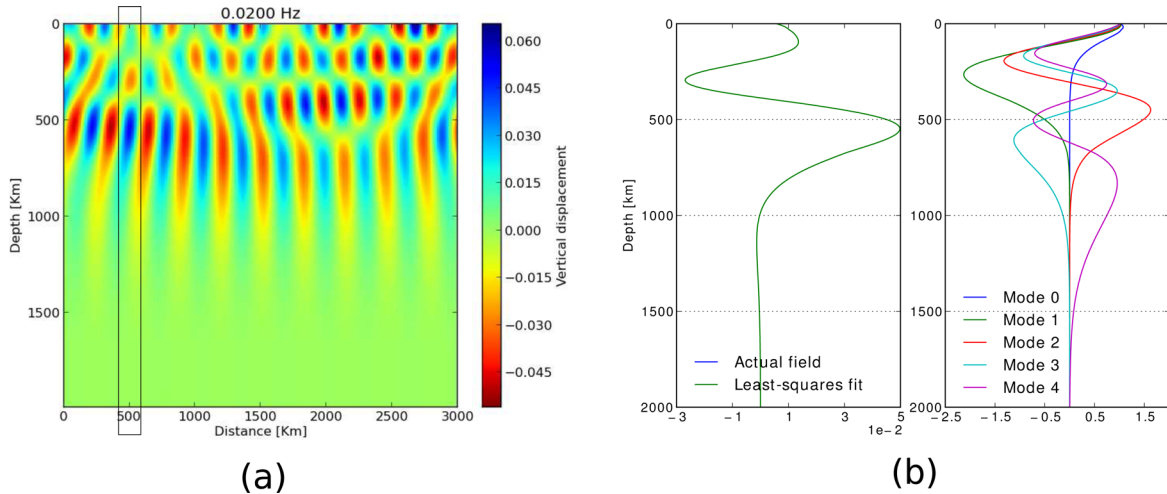
Figure 1. Example of wavefield fitting demonstrated with a known wavefield consisting of the Rayleigh wave fundamental mode and first four overtones, computed analytically in a laterally homogeneous model: (a) vertical displacement everywhere in the model at 50 s period; only the real part of the total field is shown and the thin rectangle highlights the part of the field used in part (b). (b) Fitting of the field at a single lateral position (500 km) in the model—left panel shows the total field along with the obtained fit, right panel shows the normalized Rayleigh mode eigenfunctions used to obtain the fit.

neighbour' masses and eliminating the contribution from the mass at the centre of the nine-point star. Though the resulting number of variables is significantly greater with these choices, the computation remains tractable.

2.2 Analysis of modelling results

In order to quantitatively study the phenomenon of mode conversion, it is necessary to know the modal constitution of a wavefield before/after propagation through a heterogeneity; for this a method is required to analyse and deconstruct the total field obtained by forward modelling.

2.2.1 Measurement of individual mode amplitudes

The forward solver used in this study works in the frequency domain. We exploit the fact that the field is available everywhere in the model and at each frequency, by using an unconventional analysis tool: least-squares fitting of the total field by linear superposition of surface wave modes. This idea is similar to that of Szelwis (1983), and in the context of studying a field that includes scattering from heterogeneities, is founded on assuming that the body-wave component of the scattered field is minor. The total field Φ is written as a sum of modes

$$\Phi(\omega, x, z) = \sum_m a_m(\omega)E_m(\omega, z)e^{ik_m(\omega)x} \qquad (1)$$

where x = lateral position in model; Φ = vertical profile of single component (vertical or radial for Rayleigh, transverse for Love waves) of wavefield at frequency ω, taken at location x in 2-D model; E_m = corresponding displacement component of eigenfunction of mode m at frequency ω in background model; a_m = amplitude or participation factor of mode m; k_m = wavenumber of mode m at frequency ω in background model.

Since the mode eigenfunctions represent the amplitude of particle motion as a function of depth, for clarity we use the term *mode participation factor* (MPF) to denote the strength of each mode in the total field. Determination of the MPFs $a_m(\omega)$ can be cast as an optimization problem of fitting $\Phi(\omega, x, z)$ with $E_m(\omega, z)$. Combining

the participation factor and phase terms in (1), gives

$$\Phi(\omega, x, z) = \sum_m A_m(\omega, x)E_m(\omega, z) \qquad (2)$$

where

$$A_m(\omega, x_i) = a_m(\omega)e^{ik_m x_i}.$$

Rewriting (2) in matrix notation,

$$\Phi(\omega, x) = \mathbf{E}(\omega)\mathbf{A}(\omega, x).$$

The above equation is solved for $\mathbf{A}$ in the least-squares sense by solving

$$\mathbf{E}^T\mathbf{E}\mathbf{A} = \mathbf{E}^T\Phi \qquad (3)$$

which yields the coefficients A_m at a single location x. An example of this is shown in Fig. 1. Eq. (3) is solved for a discrete number of points at locations x_i to get a set of coefficients $A_m(\omega, x_i)$. The modulus of these coefficients should be the same at each location (in a laterally homogeneous model), which suggests the use of the following estimator for the MPFs:

$$\hat{a}_m(\omega) = \overline{|A_m(\omega, x_i)|} \qquad (4)$$

where the overbar represents the mean over the set of locations x_i chosen to span one complete wavelength (longest wavelength in case of multiple modes). Variations in $|A_m|$ over the set x_i are a measure of the error (Δa_m) in the estimate for $a_m(\omega)$ (the standard deviation is used as the error estimate). The entire procedure is implemented independently for each frequency to yield the complete modal makeup of the total wavefield.

Through simple tests in laterally homogeneous (1-D) media, we have confirmed that this method is effective and accurate—it reproduces exactly the known individual MPFs (provided that fundamental influences on amplitude, namely anelastic attenuation and geometrical spreading, are suitably taken care of). In case of 2-D models, the obvious caveat associated with this method is that it can only be applied to parts of the model which are laterally homogeneous, so that the local eigenfunctions used for wavefield fitting are consistent over the set of locations x_i in eq. (4). The tests with
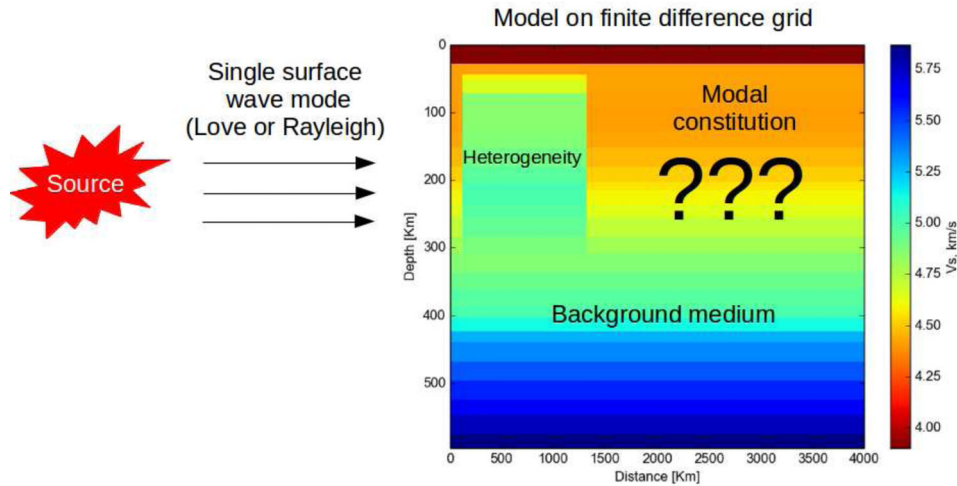
Figure 2. Schematic to illustrate the study method: there is a 2-D model discretized on a uniform grid in both directions, and a teleseismic earthquake source lying outside the model. The 2-D model consists of a 1-D (laterally homogeneous) background medium with a heterogeneity imposed on it as a percentage perturbation. The model in the source region as well as between the source and the 2-D model is equal to the background medium. Description of the canonical study model: it consists of a 1200 km wide, +10 per cent perturbation to the background model, in the depth range 44–304 km. The perturbation starts at a lateral distance of 120 km in the model. To ensure vertical smoothness, which is relevant for the inversions of Section 4 (see vertical correlation length in CL1987), the perturbation has linear vertical tapers at the top and bottom, of thickness 44 km and 100 km respectively. There are no lateral tapers, which means the lateral boundaries are sharp. Note that the velocities shown are in flattened coordinates and only the top 600 km of the model are shown.

simple 2-D models presented in Appendix A serve to validate not only the FD solutions but also this analysis technique.

2.2.2 Energy distribution among modes

The amplitudes obtained as described above depend on how the eigenfunctions used for wavefield fitting are normalized. In this study we use eigenfunctions normalized to unit surface displacement, hence the MPFs obtained are a measure of each mode's surface displacement. To calculate energies of individual modes, we compute mode amplitudes with respect to eigenfunctions normalized such that each mode transports unit energy. We do this indirectly by computing the surface wave orthogonality product defined by Herrera (1964), simplified for 2-D wave propagation with x-axis along the propagation direction:

$$\frac{1}{2}\int_0^\infty \sum_{q=x,y,z}\left[u_q^l\sigma_{xq}^{m*}-u_q^{m*}\sigma_{xq}^l\right]\mathrm{d}z = N_m^2\delta_{ml} \quad (5)$$

where u_q and σ_{xq} are the components of displacement and stress respectively, on a surface normal to the propagation direction, and l and m are mode indices. N is a constant and δ_{ml} is the Kronecker delta. Hererra's scalar product is directly related to energy flux carried by a mode, because flux is given by stress × velocity and in the frequency domain, velocity and displacement are separated only by a factor of $i\omega$, that is, the energy flux is

$$F = i\omega N^2. \quad (6)$$

This leads to the following integrals (here we have used the Aki & Richards (2002) nomenclature for surface wave eigenfunctions and dropped the mode index for clarity):

$$F = \omega k\int_0^\infty \mu l_1^2\mathrm{d}z, \quad \text{for Love modes}$$

$$F = \omega\int_0^\infty[\sigma_{xx}r_1-r_2r_3]\mathrm{d}z, \quad \text{for Rayleigh modes} \quad (7)$$

which are easily evaluated numerically using Simpson's rule. Energy-normalized eigenfunctions ϕ^E are related to arbitrarily nor-

malized eigenfunctions ϕ^u as $\phi_m^E = \phi_m^u/\sqrt{F_m}$; hence once the amplitudes of modes relative to ϕ^u are known (e.g. a_m in previous section), their amplitudes e_m relative to ϕ^E are simply

$$e_m = a_m\sqrt{F_m}$$

The set of amplitudes e_m is all that is needed to determine the modewise energy distribution of a wavefield because energy carried by mode m is simply $|e_m|^2$. In this paper, energy of modes refers to energy flux carried by modes and it is derived from FD modelling results by first computing a_m by the method of Section 2.2.1, then scaling by the appropriate norms to get e_m.

3 FORWARD MODELLING

Equipped with a tested FD solver, we proceed to analyse the nature and extent of mode conversion of Rayleigh and Love waves in a variety of 2-D models that contain lateral heterogeneities at scales currently resolvable through surface wave tomography. Given a single surface wave mode impinging on a region of lateral heterogeneity, the objective of our numerical experiments is to determine the modal content of the wavefield after transmission through the heterogeneity. Here the incident surface waves are produced by an earthquake source and the localized structural heterogeneity is at teleseismic distances (Fig. 2). This approach involves a number of variables including the specific source mechanism, the background model (on which heterogeneity is imposed) and the nature of the heterogeneity itself. However, for the stated objective, the first two are dummy controls—mode conversion is a wave propagation phenomenon, unrelated to wave excitation, and it is governed by gradients in structure rather than the actual structure itself. Therefore in this paper we present results using a single background model, and a single earthquake source chosen for convenience. The 1-D background model has its mantle structure derived from PREM (the 220 km discontinuity in PREM is smoothed), and a single-layer crust (with a view towards simplifying inversion of the simulated data in Section 4), of thickness 28 km. The teleseismic source corresponds to the 16/05/2006 M_w 7.4 event in the Kermadec

Islands region; chosen for its ~150 km depth, which ensures excitation of the fundamental mode as well as first five overtones over the frequency range of interest, and its long source time function, which ensures that the source spectrum (and therefore that of the background wavefield) does not have appreciable amplitude at frequencies higher than are modelled by FDs. Any other source may be used without fundamentally affecting the results of this paper.

In this way the experiment reduces to studying the effect of variations in the nature of the lateral heterogeneity only. Even so, a large number of possibilities exist—the shape, lateral extent, vertical extent, strength, sharpness and depth of the perturbation can all be varied independently. A further simplification is made in that only the strength, lateral extent (width) and the sharpness of the perturbation are varied. While all geometrical parameters of the heterogeneity would affect mode conversion, the essential physics of the process can be captured by varying only the three aforementioned parameters (strength, width, sharpness), provided the rest are sensibly chosen to approximate realistic upper mantle heterogeneities. Therefore we define a *canonical study model* (see Fig. 2), from which all other study models are derived by varying any combination of the three chosen parameters.

3.1 Experiment details and analysis of output

FD modelling is done with a model size of 4000 km (width) by 2800 km (depth) using a grid spacing of 4 km. Modelling is restricted to a highest frequency of 0.08 Hz (12.5 s period), which for the chosen grid corresponds to a sampling density of ~12–14 grid points per shortest wavelength (GPPSW). The numerical experiment (Fig. 2) is done separately for each incident mode—from the fundamental to the fifth overtone—and separately for Rayleigh and Love waves. Attenuation and geometrical spreading are excluded from the modelling (turned off) to allow the implementation of the wavefield fitting technique described in Section 2.2 without having to worry about how far beyond the heterogeneity the measurements are made. The earthquake source, which generates the background (incident) field, is an arbitrary distance outside the model.

To quantify the results of each simulation we compute the transmission surface ratio, Y (see Appendix A), and the fraction of incident energy, T_E, carried by transmitted modes. Techniques for doing so have been fully described in Section 2.2 but we note that, given the nature of the study models, measurements of the transmitted field beyond the model heterogeneity are in the same medium as that of the unperturbed incident field. Because the incidence-side and transmission-side media are the same, 'transmission coefficients' for any given mode transmitting into itself cannot be greater than unity (unlike Fig. A4 where transmission from one type of medium into another is considered, allowing transmission coefficients greater than unity). With this caveat and using subscripts m, i as general and incident mode indices respectively, Y and T_E are computed as follows:

$$Y_m^i = \frac{a_m}{a_i}$$
$$T_{E,m}^i = Y_m^{i\,2} \left(\frac{F_m}{F_i} \right). \tag{8}$$

The wavefield fitting process is not exact—there is error in a_m, leading to errors in Y and T_E which are computed as:

$$\Delta Y = \Delta a_m \left(\frac{Y}{a_m} \right)$$
$$\Delta T_E = \pm 2 \frac{T_E}{Y} (\Delta Y) + \frac{F_m}{F_i} (\Delta Y)^2. \tag{9}$$

This formulation for error propagation is founded on treating a_i and F as error-free constants, which they are in theory. In practice a_i is still error-free as it is measured in the laterally homogeneous background model, but the quantities F contain some errors due to numerical integration of discretely sampled eigenfunctions. We minimize these errors by sampling the eigenfunctions densely enough so that F_m is practically equal to energy density × group velocity, for all modes considered (energy density computed using standard energy integrals for Love/Rayleigh waves). However a correction is made to account for the fact that modes other than the single input mode are measured even in the absence of any model heterogeneity. These 'spurious modes' are artefacts of model discretization (Appendix B) that contaminate measurements in the heterogeneous case, and so are factored in to the formulation represented by eqs (8) and (9). The amplitude of spurious modes which are measured in the background model (during measurement of a_i) is treated as an error in the measurement process and added to the inherent error in a_m. Quantitatively, this means that the Δa_m in eq. (9) is

$$\Delta a_m = \Delta^0 a_m + a_i^m \tag{10}$$

where $\Delta^0 a_m$ is the inherent error in the wavefield fitting technique and a_i^m is the amplitude of mode $m(\neq i)$ obtained when a measurement is made in the 1-D background model with mode i being the only input.

Finally, because their amplitudes are small in the models considered, no modes beyond the 10th overtone are used in the fitting (at any frequency, all the modes that exist up to the 10th overtone are used). This exclusion of higher modes may lead to a less complete picture of modal constitution, but it is not an incorrect one.

3.2 Results for individual models

We first present results for the canonical study model; results for all other models are presented in a similar format. Love wave results for the canonical study model (Fig. 3) show that the fundamental mode propagates largely unchanged, with little conversion to other modes. However, higher modes show significant conversion to other modes, including the fundamental, when they are incident. The conversion is evident from wavefield decomposition as well as dispersion measurement from waveforms, the latter providing an indirect representation of the contribution of each mode to the total field. Note that in each incident mode case, the total transmitted energy in all the modes used for fitting adds up to roughly the single-mode incident energy.

The canonical test model with its 10 per cent perturbation and sharp lateral boundaries represents the most severe case of lateral heterogeneity considered in this study and with a preview of its results, we now move on to models with weaker heterogeneity as shown in Fig. 4. Either the strength of the perturbation is reduced, keeping the boundaries sharp, or the (maximum) strength is held fixed at 10 per cent and the lateral boundaries are smoothed using symmetrical linear tapers within which the perturbation changes linearly between 0 and the maximum. Exactly the same kind of models but with a negative perturbation instead of a positive one, are also considered. A nomenclature is used to name the different models (see Fig. 4), for convenient reference throughout the rest of the paper, including reference to other similar models which are not shown.

Figures for all the study models are provided in the Supporting Information. They provide a lot of model-specific detail but some of the key observations are: for positive perturbation models the fundamental mode suffers negligible conversion as compared to
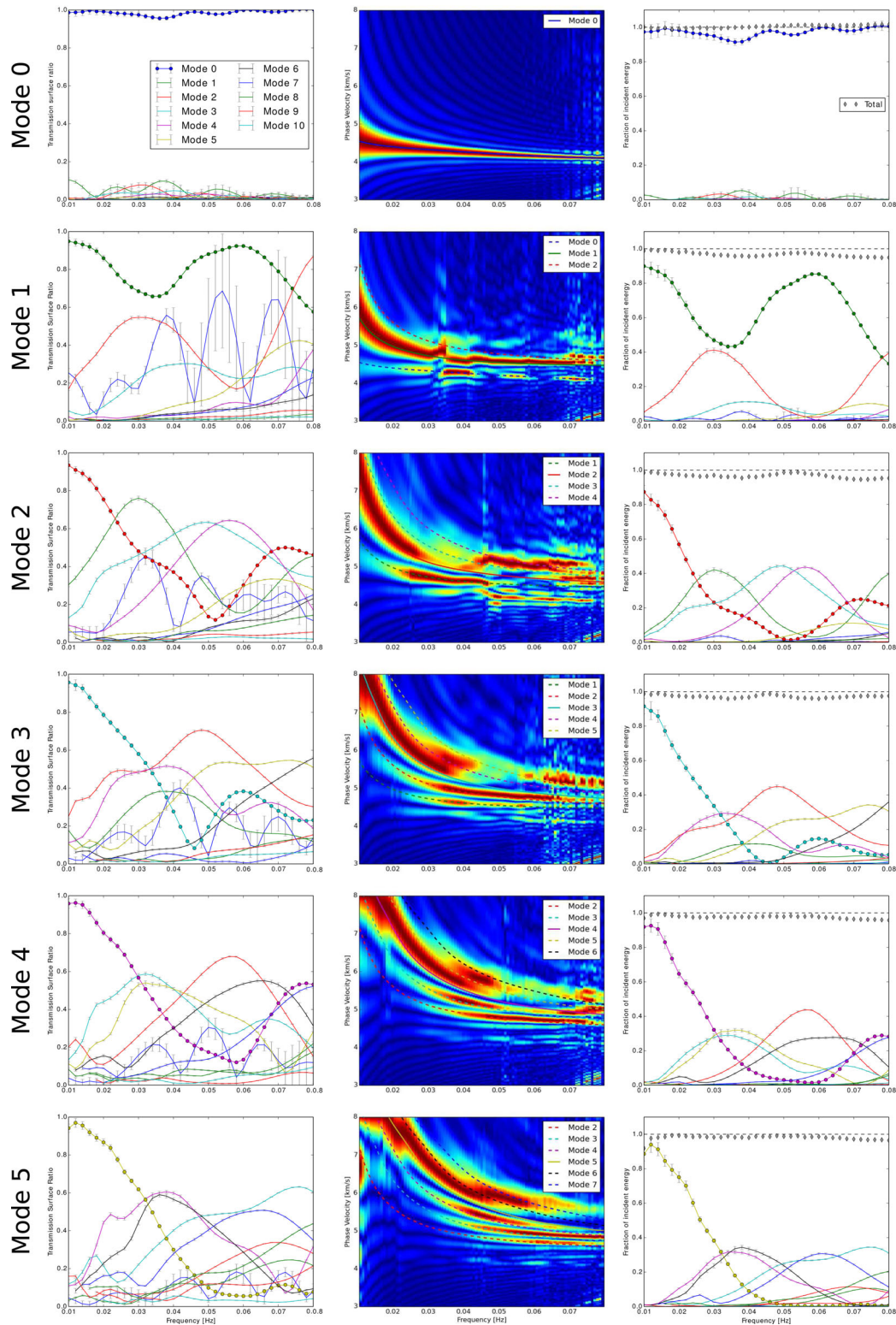
Figure 3. Love wave results for the canonical study model. The 6 rows from top to bottom correspond to incidence of mode numbers 0 through 5 as indicated on the left hand side. Left and right panels: transmission surface ratio and energy transmission respectively—the colour scheme showing different modes is common to the two panels and is used throughout this section; the incident mode is distinguished by a line with circular markers as opposed to line only. In the energy plots on the right, energies of individual modes (relative to incident energy) are added up to produce the total energy transmission coefficient, shown by grey diamonds. The conspicuous suppression of the fundamental mode in these plots shows that although the fundamental mode has appreciable surface amplitude in the transmitted field, it accounts for very little of the incident energy. Middle panel: phase velocity dispersion measured by the simple slant-stack method (e.g. Park *et al.* 1998; Van der Kruk *et al.* 2007; Douma & Haney 2013) using waveforms at 'stations' (placed every 60 km) on the transmission side. Here the colour scheme for individual modes is the same as in the two side panels, but the incident mode is distinguished by a solid line whilst other modes are shown by dashed lines. There is good correspondence between the measured dispersion and the transmission surface ratio.
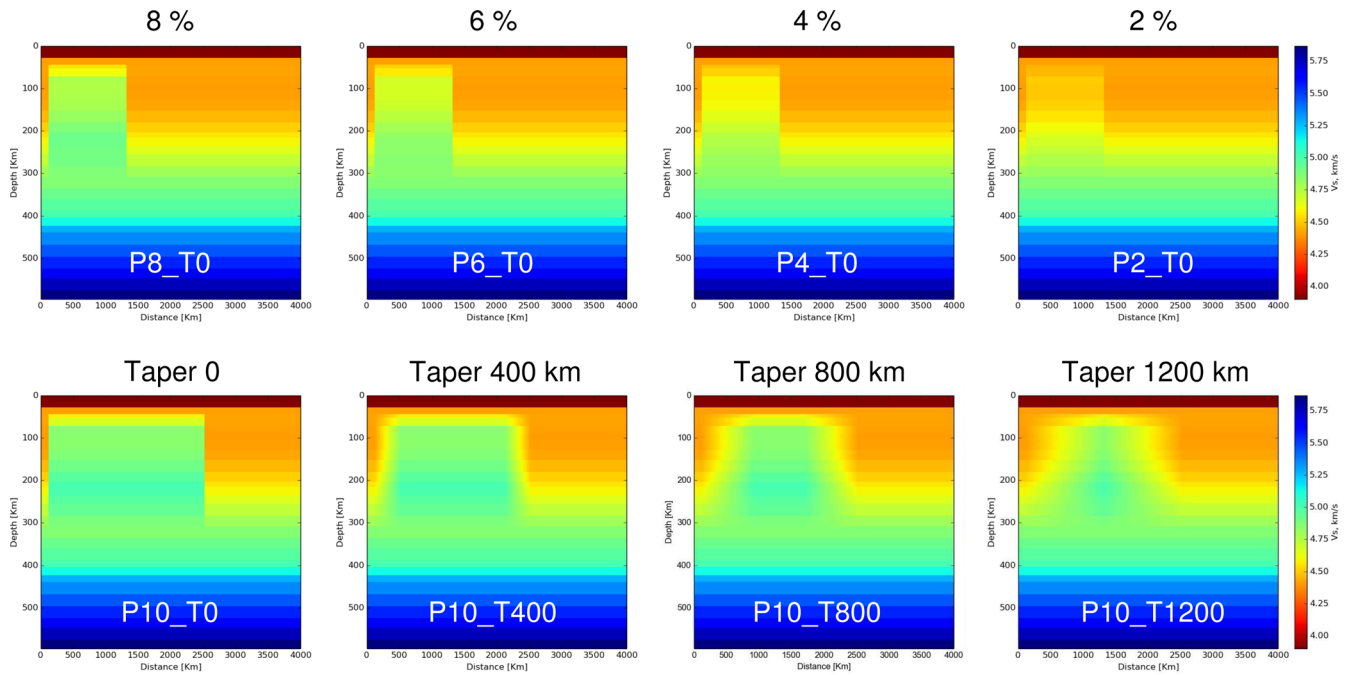
Figure 4. Study models used in this study. Varying degrees of lateral heterogeneity are achieved by varying either the perturbation strength (with sharp boundaries, top row) or the smoothness of the lateral boundaries (with 10 per cent strength, bottom row). Note that in the bottom row the total width of the heterogeneity is increased to allow for smoother lateral boundaries. The generic format of model names is <X><S>_T<L1>_W<L2>. Here <X> is either 'P' or 'N', indicating a positive or negative perturbation respectively; <S> is an integer denoting the percentage strength of the perturbation and <L1> is the length in km of the lateral taper on either side, and <L2> is the total width of the perturbation. In this study we are interested in the strength of heterogeneity <S> and the length-scale <L1>; the length-scale <L2> is of secondary importance and is only varied to allow the desired range on <L1>.

the overtones; conversion of/to the fundamental mode is generally greater for Love waves than for Rayleigh waves; conversion of/to the fundamental mode is significantly greater for negative perturbation models (up to 95 per cent of incident energy converted in case of Love waves) than for positive perturbation models (at most 15 per cent of incident energy converted).

The single-incident-mode approach taken in this paper reveals rather complex mode conversion behaviour, with a single mode giving rise to multiple other modes with varying strengths as a function of frequency. However in order to study what happens in the real Earth, one may wish to take a comprehensive view—what is the net effect of a mixture of modes interacting with a heterogeneity? We have seen that a single incident mode loses energy to other modes by conversion but that same mode is also likely generated by conversion from a different incident mode. Hence the net effect of a heterogeneity on the modal constitution of an incident wavefield containing a mixture of modes (as in the real Earth), remains obscured in the mode-wise picture. But we can combine the mode-wise results into a comprehensive result for each model—this is most easily done in terms of energy because energies in different modes can simply be added. Thinking of the incident field as a mixture of modes, we compute the total transmitted energy in mode m, $E_m(\omega)$, by adding up its energy in the transmitted field from each single-mode-incidence case

$$E_m(\omega) = \sum_{i=0}^{5} T_{E,m}^i(\omega) E_i(\omega) \qquad (11)$$

with E_i being obtained from a_i as $a_i^2 F_i$. We do this for $m \in [0, 5]$ only, that is, the comprehensive picture of the transmitted field is

limited to those modes which were incident. Error propagation in the above equation is straightforward:

$$\Delta E_m(\omega) = \sum_{i=0}^{5} E_i(\omega) \Delta T_{E,m}^i(\omega). \qquad (12)$$

Results are presented in such a way that energies are normalized at each frequency, that is, at each frequency we look at the percentage of the total energy carried by each mode. Doing this for the incident and transmitted fields shows how the energy partitioning (among modes) of a surface wavefield, is altered by propagation through a heterogeneity. A Love wave example (Fig. 5) shows a clear correlation of the extent of energy redistribution, with strength of model heterogeneity. Note that the grey stars in this figure, which show the sum of modal energies, start out near the 100 per cent mark at the low frequencies but drop well below this level at higher frequencies—this is a reflection of the fact that at low frequencies the total incident energy is contained in the same modes that were incident, but at higher frequencies, a significant proportion of it is lost to higher modes not included in the comprehensive result. Figures of this kind can be made for all study cases, but they have the limitation that they contain an imprint of the source excitation—the energy distribution of the incident wavefield is tied to the particular earthquake source used in this study—so they are not used beyond the simple qualitative summary provided, for example, by Fig. 5.

3.3 Overview and comparison with noise

In order to quantify the significance of mode conversion as a function of medium heterogeneity, we go back to the mode-wise picture and compare converted mode amplitudes with typical noise levels in seismology. Absolute values of these amplitudes of course
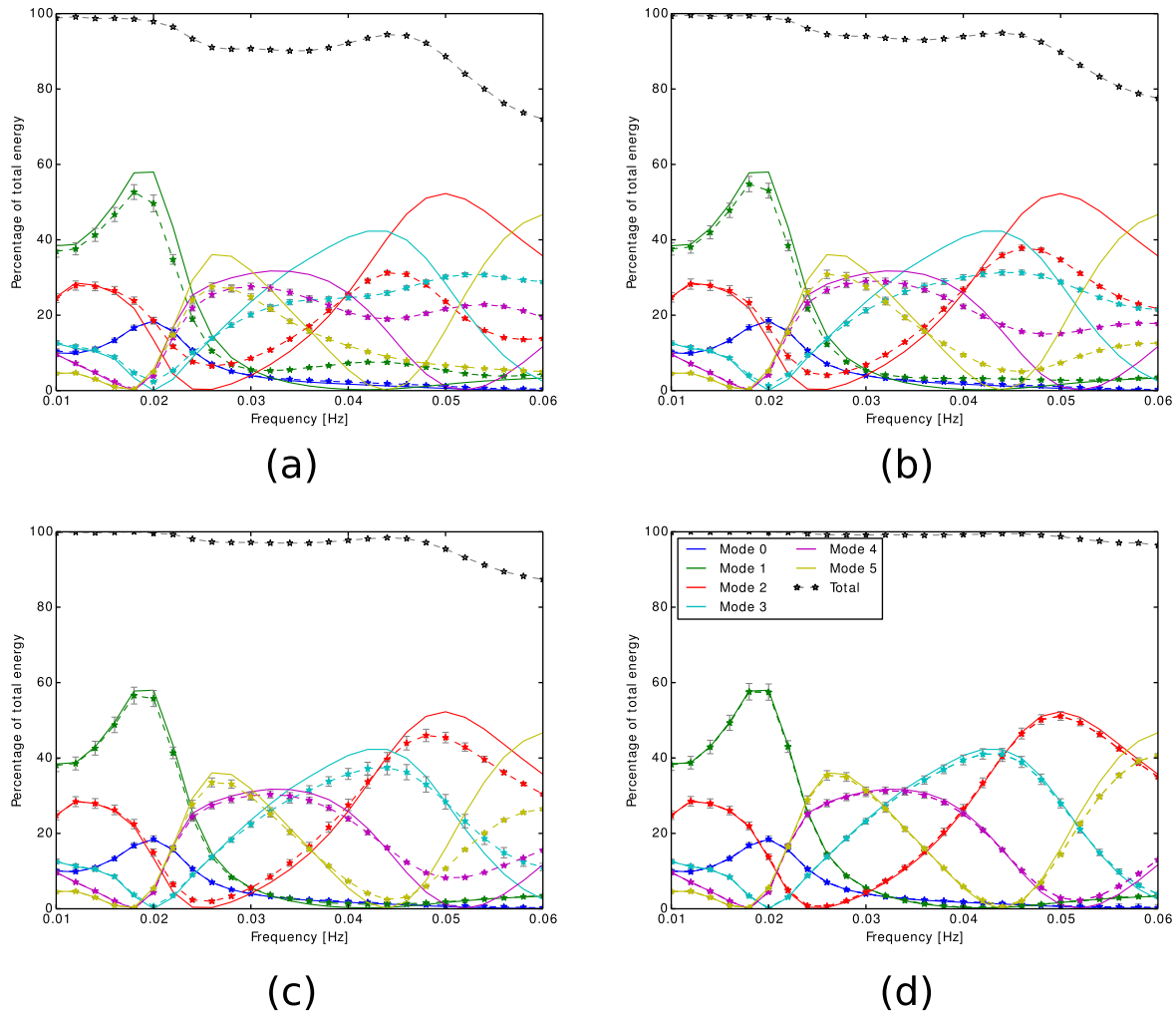
Figure 5. Love wave comprehensive result for models (a) P8_T0 (b) P6_T0 (c) P4_T0 (d) P2_T0. In each plot the solid lines show the incident field energy distribution; dashed-starred lines show energies in the transmitted field, using the same colour scheme. The grey stars at the top denote the sum of the energies of the 6 modes considered, in the transmitted field. The details of this figure, i.e., the shapes of the solid lines, are tied to the excitation characteristics of the particular source used and are unimportant; its main purpose is to illustrate the deviation (or lack thereof) of the dashed-starred lines from the solid lines.

depend on the amplitude of the 'incident' wavefield, which depends on extraneous factors (unrelated to medium heterogeneity)—predominantly source strength and distance from source. The greater the earthquake magnitude and smaller the epicentral distance, the stronger (in absolute terms) will be the effects of mode conversion. Here we use a single scenario as an example, with the knowledge that the results will simply scale with the two aforementioned factors.

So far this paper has been concerned only with relative quantities: surface amplitude or energy transmission coefficients. To convert these to absolute values, one only need invoke the amplitude of the incident field. Thus far absolute amplitudes have been unrealistic because all computations have been performed *without* attenuation and geometrical spreading; now for this summary section we recompute the background wavefield using a simple attenuation model ($Q_P = Q_S = 590$ at all depths), allowing for geometrical spreading and placing the earthquake source at a distance of 3000 km outside the FD model. We refer to the recomputed background field taken at the start of the FD model as *the incident field* in the remainder of this section. Note that this approach for computing absolute amplitudes *beyond the model heterogeneity* is approximate because it does not account for the amplitude reduction (due to spreading and attenu-

ation) as the heterogeneity is traversed. Finally, the specific choice of source distance and *Q*-value used in this section is somewhat arbitrary, but it is consistent with the next section where synthetic waveforms subject to inversion are generated with exactly the same set up.

In this way we have a means of obtaining absolute amplitudes of mode conversions, for one particular scenario which is a realistic example in global surface wave tomography. In order to compare these to known noise levels in seismic records, we use the USGS New Low Noise and New High Noise Models (NLNM and NHNM respectively) constructed by Peterson (1993). These models may be seen as lower and upper bounds on Earth noise manifested in seismic records. They are popularly used in the form of power spectra for ground acceleration; here we use them as amplitude spectra for ground displacement (for easy comparison with surface amplitudes of modes), with the amplitude spectrum being simply approximated by taking the square root. Once converted to absolute amplitude, we find that for the particular source and distance used, the incident field itself is of lower amplitude than the (high) noise model at some frequencies, especially for the higher modes.

With this background we consider the summary figures of this section. So far in this paper, figures have corresponded to a

single model studied over a range of frequencies; now figures are made using a range of models at a single frequency. The aim is to visualize the effects of different heterogeneity parameters and generalize the results beyond the specific study models used, so for each incident mode and any given frequency, the transmission surface ratio is plotted against some non-dimensional parameter representing the medium heterogeneity—this may be the perturbation strength (per cent perturbation with respect to background) or the smoothness length scale (*D*) relative to the seismic wavelength λ. Ultimately the results are still presented in relative form but the comparison with noise is achieved by scaling the noise models relative to the incident field amplitude.

The results for both Love and Rayleigh waves in negative perturbation models (Figs 6 and 7; a comparison between these validates the earlier claim of greater fundamental mode conversion in the Love wave case) show gross signs of mode conversion decreasing with model smoothness, though these are not directly obvious. Only some of the plots (e.g. mode 2 incidence in the Love case or mode 1 incidence in the Rayleigh case, at 33 s period) show the incident mode regaining its original amplitude, whilst converted modes decline in amplitude, with increasing smoothness. However with these plots there is a danger in looking at each frequency in isolation. For example in the Love wave case (Fig. 6) at 20 s period, conversion from the fundamental mode to the first overtone or vice versa, appears to amplify with increasing smoothness in the first four models. This does not mean that mode conversion at the short periods gets stronger with increasing model smoothness. To understand this it is necessary to look at the complete result (Supporting Information)—in the sharpest model, conversion from mode 0 to mode 1 has a peak at ∼0.065 Hz; as the model gets smoother this peak moves towards the lower frequencies (and eventually diminishes in amplitude), thereby causing increased converted amplitude at 0.05 Hz or 20 s period. The move towards lower frequencies reflects the fact that a given model smoothness may be 'smooth enough' for the high frequencies (shorter wavelengths) but not so for lower ones. Nonetheless it may be argued that at 20 s period for example, $D \approx 15\lambda$ is still sharp enough to produce significant mode conversion (given a maximum model perturbation of 10 per cent). Fortunately the critical value of D/λ reduces with frequency (increasing λ): at 33 s, $D \approx 12\lambda$ and at 100 s, $D \approx 3\lambda$ may be deduced as being smooth enough for negligible mode conversion.

Results from variations in heterogeneity strength rather than smoothness (Supporting Information) exhibit a clearer trend of converted mode amplitudes increasing with heterogeneity strength at all periods. At 100 s period, conversions from all modes are below the high noise level (considering cases where the incident mode amplitude is above the noise level), with the incident mode showing negligible departure from its original amplitude. At shorter periods where conversions are stronger it can be argued that a heterogeneity of 2 per cent strength is too weak to produce conversions above noise levels, but 4 per cent heterogeneity is strong enough for the same—at 4 per cent one can just see the incident mode falling below its incident amplitude. At 6–8 per cent and above, conversions are strong enough to rise above the incident amplitude.

Irrespective of heterogeneity strength and smoothness, a key observation in this study is that conversion of the fundamental mode is insignificant—well below noise levels—at all periods, at least for Rayleigh waves (the Love wave fundamental shows significant conversion in negative perturbation models). This bodes well for surface wave studies based on fundamental mode phase or group velocity dispersion (e.g. Trampert & Woodhouse 1995; Ekström *et al.* 1997; Nettles & Dziewoński 2008). However, higher-mode

analysis provides added resolution of the shallow structure and is required to resolve deeper upper mantle structure.

4 WAVEFORM INVERSION

The analysis in the previous section shows that there can be significant energy in converted modes, to the point that they may be identified in actual seismograms and exploited in imaging algorithms. A related question is the extent to which ignoring the existence of mode conversions biases the wave-speed models generated by inversion algorithms that make use of higher mode observations. In other words, to what extent can one afford not to explicitly model mode conversions when constructing models of the subsurface? The effects of such 'model induced error' on an inverse algorithm are not easy to quantify in a general way, since the extent to which an algorithm is robust to them can depend on factors such as details of the recording geometry or choices of how a system of equations is conditioned. Nevertheless, we can obtain some insight into the effects of ignoring mode conversions by considering how they influence the observations that are used in the inverse problem.

We take as an appropriate and illustrative example the multimode inversion algorithm of CL1987 as implemented by Debayle & Ricard (2012), in part because it has been used in several regional (e.g. Debayle & Kennett 2000; Priestley & Debayle 2003; Heintz *et al.* 2005; Maggi *et al.* 2006; Priestley *et al.* 2006, 2008) and global (e.g. Debayle *et al.* 2005; Priestley & McKenzie 2006, 2013) upper-mantle studies. However, we emphasize that the mode coupling we focus on in this paper is not tied to the CL1987 inversion method but affects in a similar way any surface waveform inversion method using a modal summation in the forward calculation. The ultimate objective of the CL1987 algorithm is to determine a best-fitting, 1-D, 'true path-average' model of V_s between a given source and receiver. Critical to the application of this algorithm is the accurate identification of multiple modes in an observed seismogram. Details are available in Debayle & Ricard (2012, hereafter DR2012), but basically, modes are identified by cross-correlating the observed seismogram with synthetics generated by single modes in a reference 1-D model. The lag time (phase), amplitude, and width of the lobes that result from (taking the envelopes of) this cross correlation serve as 'secondary observables' that the algorithm then inverts to recover a true path-average model. Our primary objective in this section is to investigate the extent to which the presence of unmodelled mode conversions alters the estimates of these secondary observations.

We invert only the vertical component (Rayleigh) waveforms computed for the 2-D study models of the previous section, but with geometrical spreading and attenuation now included and with each waveform built from the combined solutions of all input modes (rather than considering each mode separately). Inversion is done with the DR2012 code appropriately adapted for use with the synthetic data of this study[1] and with the background model of the

---

[1] The *a priori* information imposed on the solution, namely the source region model and the crustal part of the solution, are taken to be equal to what was used in the generation of the synthetic data rather than being taken from third party models; attenuation (log *Q*) is eliminated as a model parameter to be inverted for; the 1-D forward solver that is tied to the original DR2012 package (based on the method of Takeuchi & Saito (1972) and Cara (1978)) is replaced by the method used to compute the background wavefield in this study (Section 2.1).
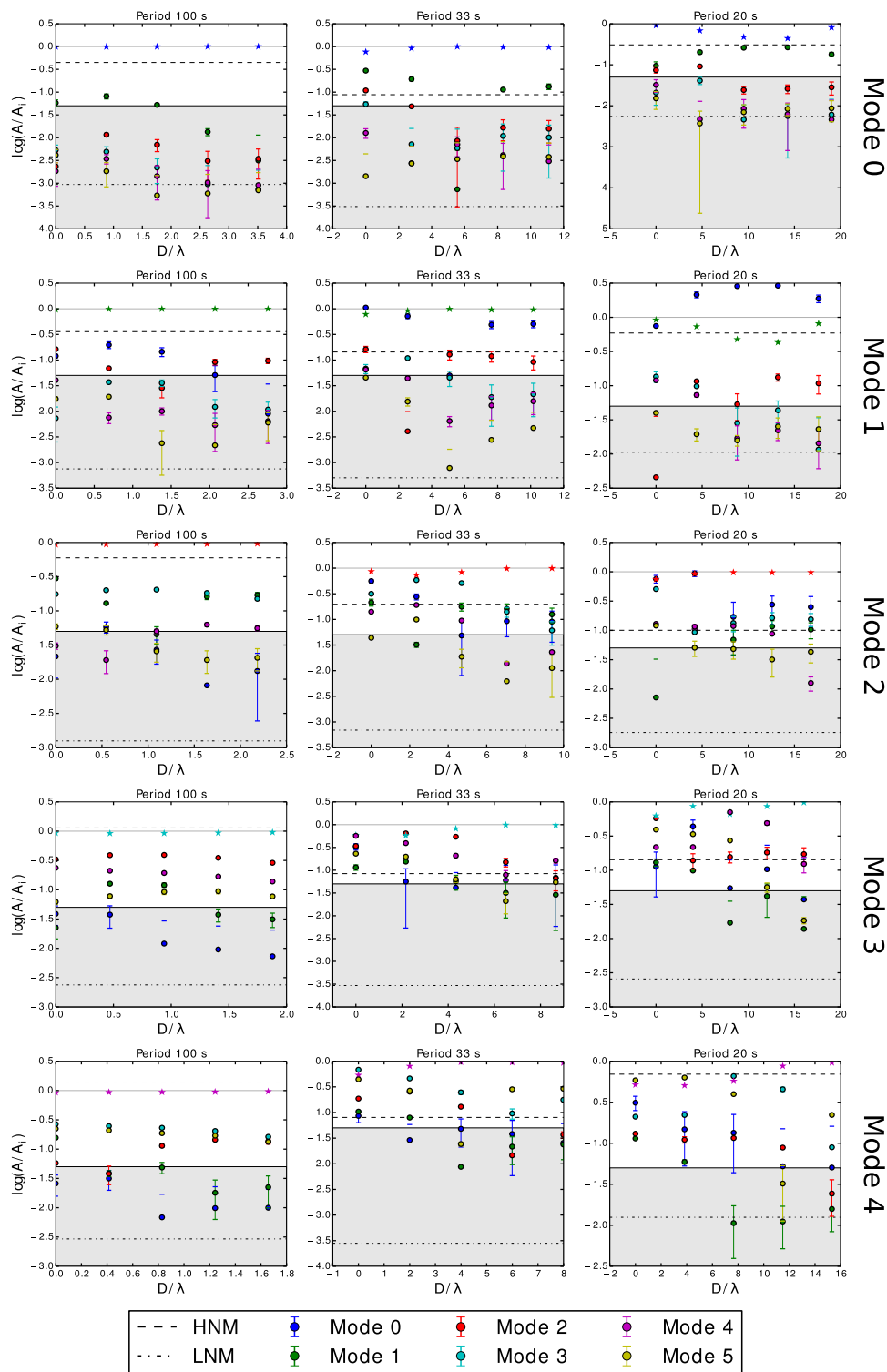
Figure 6. Love wave mode conversion as a function of model smoothness, shown for three different periods and each incident mode as indicated on the right-hand side. Note that the case of mode 5 incident is left out due to constraints of space. Models included: N10_T0_W3200, N10_T400_W3200, N10_T800_W3200, N10_T1200_W3200 and N10_T1600_W3200. Description of individual plots—for any chosen period, the log of the transmission surface ratio is plotted against a non-dimensional parameter, D/λ, representing the model heterogeneity. Here D is the length of the heterogeneity lateral taper and the wavelength λ, is that of the incident mode (denoted by stars) in the background model. Other (converted) modes are shown by circles though the colour scheme is consistent throughout. The two noise models HNM and LNM are marked by dashed lines as shown. A grey line marks the value 0 on the y-axis, representing the incident mode amplitude. Finally, the figure is grey-shaded below the y-value of -1.3, which corresponds to transmitted amplitude $\approx 1/20$th of incident amplitude. This partly arbitrary choice is based on the premise that a transmission surface ratio of 0.05 or less is hard to distinguish from the 'noise' associated with the FD modelling—see discussion on spurious modes in Appendix B. Although most plots extend well below the y-value of -1.3 to accommodate the LNM, shading is provided to draw the eye to what lies above it.
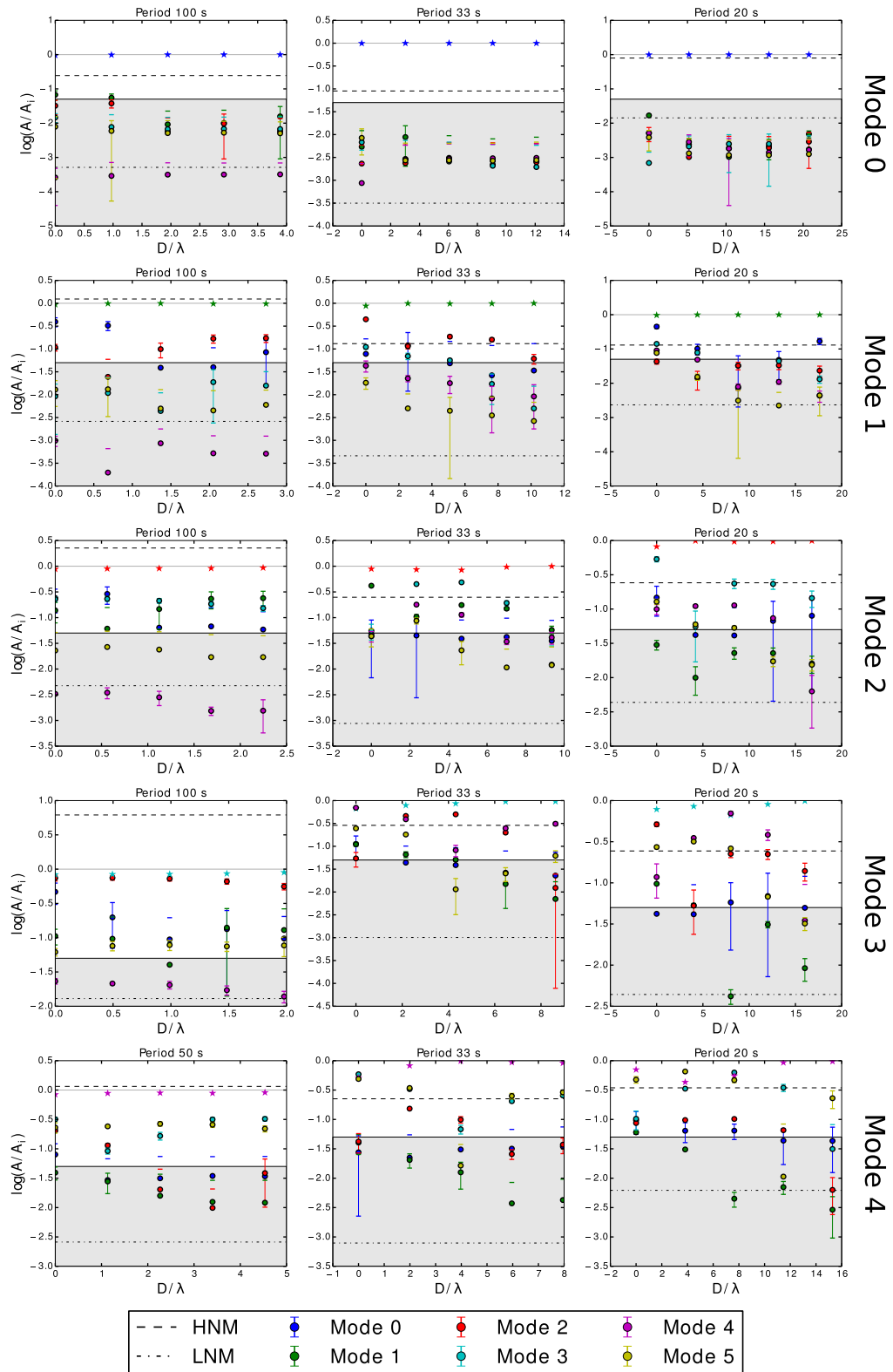
Figure 7. Same as Fig. 6 but for Rayleigh waves.

FD calculations used as the starting and reference model for inversion. To study the effects of mode conversion, we conduct a series of tests as follows: given the locations of a source and receiver in a 2-D study model, we calculate the 1-D, true path-average (TPA) model for that receiver and analytically compute 'path-average' (PA)

seismograms in this TPA model (Fig. 8). The TPA model for any receiver depends on the nature of the 2-D model heterogeneity and the fraction of the total path length between the source and receiver that passes through the heterogeneity. Both the PA seismograms and those computed by FD analysis in the 2-D model are subjected
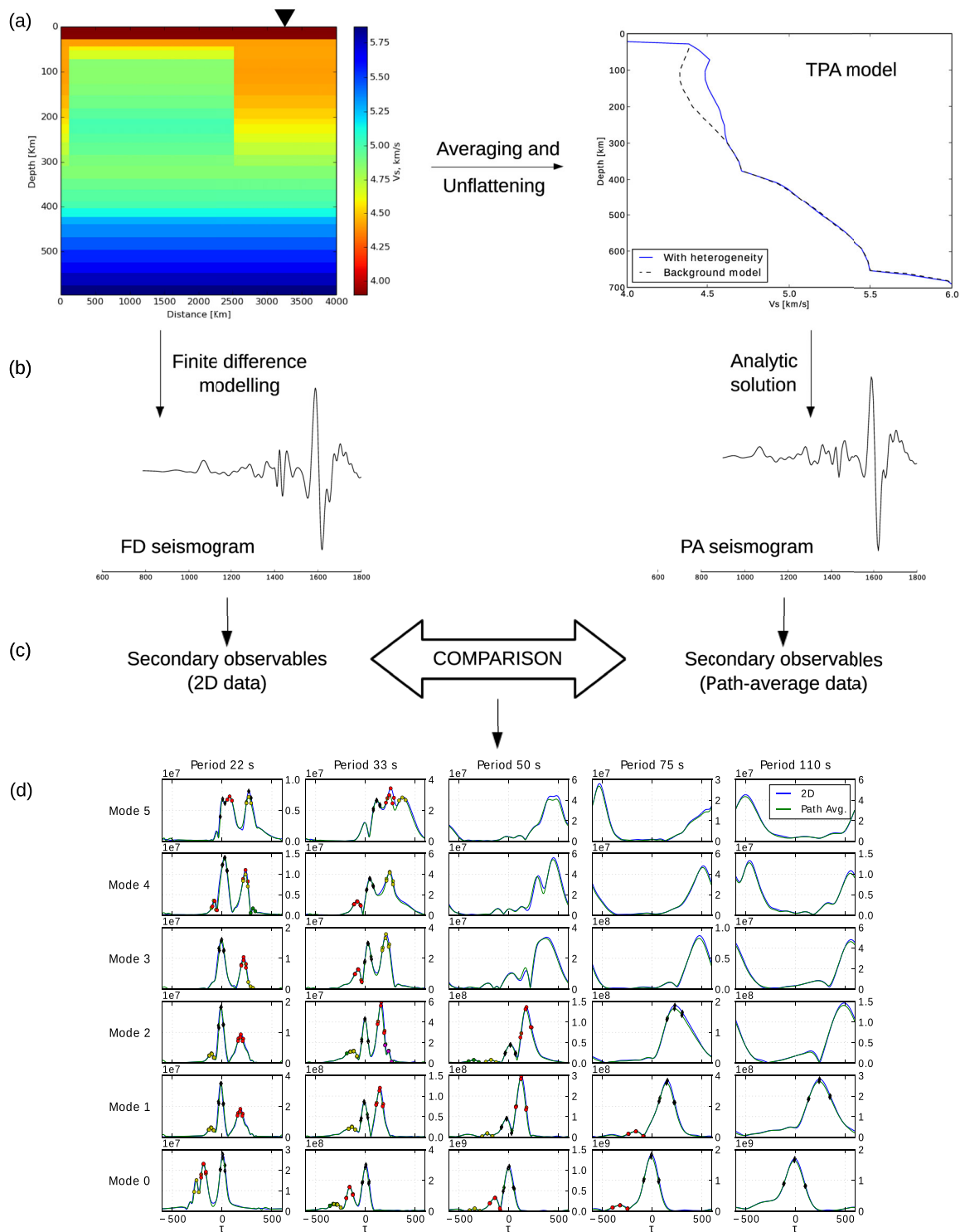
Figure 8. Schematic to explain the procedure for DPA analysis on vertical component synthetic waveforms. (a) Starting with a 2-D model as shown on the left, the true path-average V_s structure for any station (black inverted triangle) is computed (right). Averaging is done from source to station so it includes the distance of the source outside the 2-D model, which is not shown. Note that the resulting path-average structure differs from the background structure only in the depth range corresponding to the heterogeneity in the 2-D model. (b) A waveform is computed analytically in the path-average model for the same epicentral distance as in the 2-D model. (c) The two sets of waveforms are subjected to waveform inversion in exactly the same manner, and the secondary data extracted from them are compared. (d) Example of DPA analysis, using an example station lying beyond the heterogeneity in model P2_T0_W2400, which serves as a benchmark for the DPA analysis. This figure shows the envelopes of modal cross-correlograms for the 2-D data (blue curves) as well as path-average data (green curves) for the station in question. Each subplot shows the envelope(s) plotted as a function of cross-correlation time shift τ, along with the picked secondary observables (data) shown by the coloured markers—three samples for each lobe picked, one at the centre (location of maxima) and two on either side. Mode-period combinations where there are no markers have not been used in the inversion. In terms of DPA analysis, the blue and green curves showing the two sets of modal envelopes are very similar.
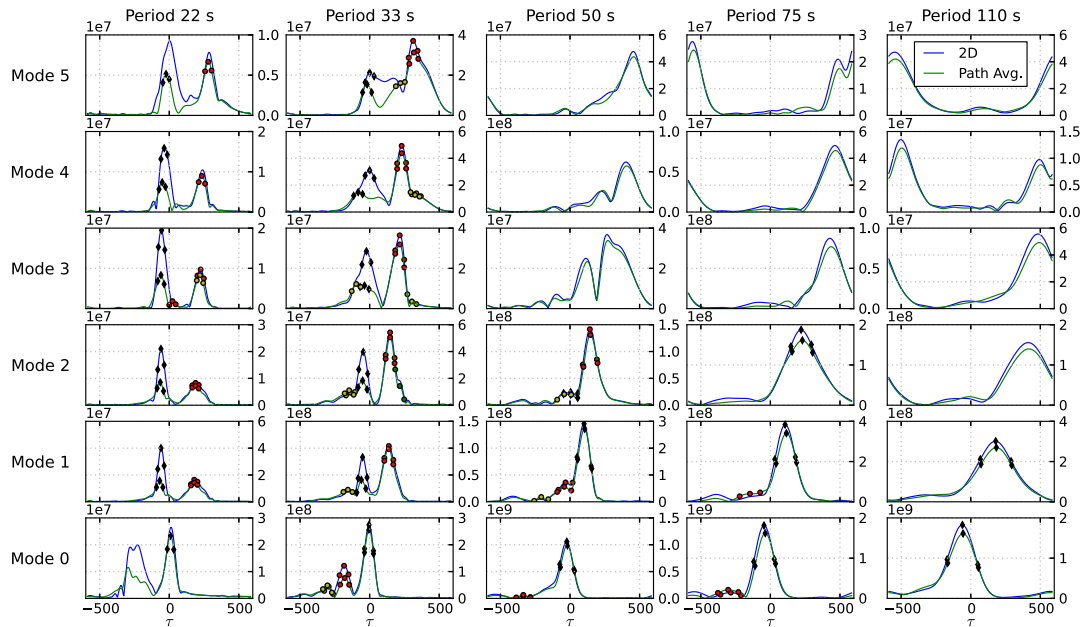
Figure 9. DPA for a 'far' station (station 46, at 3180 km in model) in model P10_T0_W2400. We use this model as a case study in this section because it permits the conduct of DPA analysis as a function of heterogeneity strength as well as smoothness. The same plotting conventions are used as in Fig. 8, but here the DPA is much higher, with significant amplitude and shape differences between the two sets of modal envelopes.

to the same mode-identification by cross-correlation technique of CL1987. We define a *Departure from the Path-Average Approximation* (DPA) as the extent to which the modal correlograms for any particular mode differ between these two. As all other things are equal, any such difference should be due to the presence of wave propagation features in the FD seismograms that are not accounted for in the PA seismograms. Hence, the DPA quantifies the extent to which the occurrence of mode conversion violates the path average approximation and alters the fundamental observable in the inverse problem.

A few examples of these tests are illustrative. First, as may be expected, in the case of weak (2 per cent) heterogeneity (Fig. 8), the modal correlograms for the PA and FD seismograms are virtually identical and the DPA is small. If we increase the level of heterogeneity to 10 per cent (Fig. 9), the DPA increases substantially, both in amplitude and phase, particularly at shorter periods (<50 s) and at higher modes. If we maintain that level of heterogeneity but reduce the sharpness of the transition (Fig. 10), the DPA decreases—particularly for phase (lag time)—in accordance with Woodhouse (1974). To summarize the results of a large number of similar test cases, we find that in general:

(i) DPA is small when heterogeneity is less than about 6 per cent but then increases with increasing percentage strength.
(ii) DPA decreases with increasing smoothness of heterogeneity. For example, DPA is not significant when the smoothness length scale, $D/\lambda \approx 8$ or larger at about 30 s period.
(iii) DPA is less for nearer stations (stations lying within the heterogeneity), than for those at larger distances (beyond the heterogeneity).
(iv) DPA decreases with increasing period, with lower DPA at periods of 50–250 s, and higher DPA for periods of 22–50 s.
(v) DPA is greater for higher modes than for the fundamental mode and lower order overtones.

Given what we have seen about the factors governing mode conversions, these trends support our contention that DPA is controlled

primarily by the strength of these conversions. Our deconstruction analysis, where we deconstruct the modal envelopes to assess the contribution of different modes, has shown that the DPA is the result of the complicated interaction of modes emanating from the seismic source and modes 'generated' by scattering at the boundaries of the lateral heterogeneity. This modal interaction distorts the propagation of the mode emanating from the source and can cause artefacts in the seismic structure derived from the typical surface wave analysis employed in multi-mode surface wave tomography. Because of this complex interaction, it is not possible to formulate simple rules for highest frequency and mode number that may be used for multi-mode surface wave analysis under the path average framework. Nonetheless Fig. 11 provides a graphical summary of the variation of DPA in this study, with frequency and mode number. What we can say with confidence is that in the presence of a laterally varying structure, the fundamental mode follows the path average approximation well but the overtones follow it less well. Extending the surface wave analysis to too high a frequency and too high a mode number can lead to a biased result which may not only affect the deep structure but may potentially corrupt the shallow structure.

4.1 Implication for inversion results

As mentioned above, the effects of these DPA errors on the outcome of an inversion (ideally the TPA model) can depend on a variety of choices in how the inversion is performed. Nevertheless, we can make some useful inferences. A simple observation is that a lag mismatch in the correlograms will translate into an error in the inferred group velocity. For example, the 33-s modal envelopes for the fourth higher mode shown in Fig. 9 have a clear mismatch of about 100 s for the left-most lobe. Given the epicentral distance of this station (6200 km), this difference in lag time corresponds to a group velocity discrepancy of ~7 per cent. Note that the model in this example has a high percentage heterogeneity (10 per cent) and a sharp lateral boundary; hence this discrepancy will be at the high end of those that we observe in our tests.
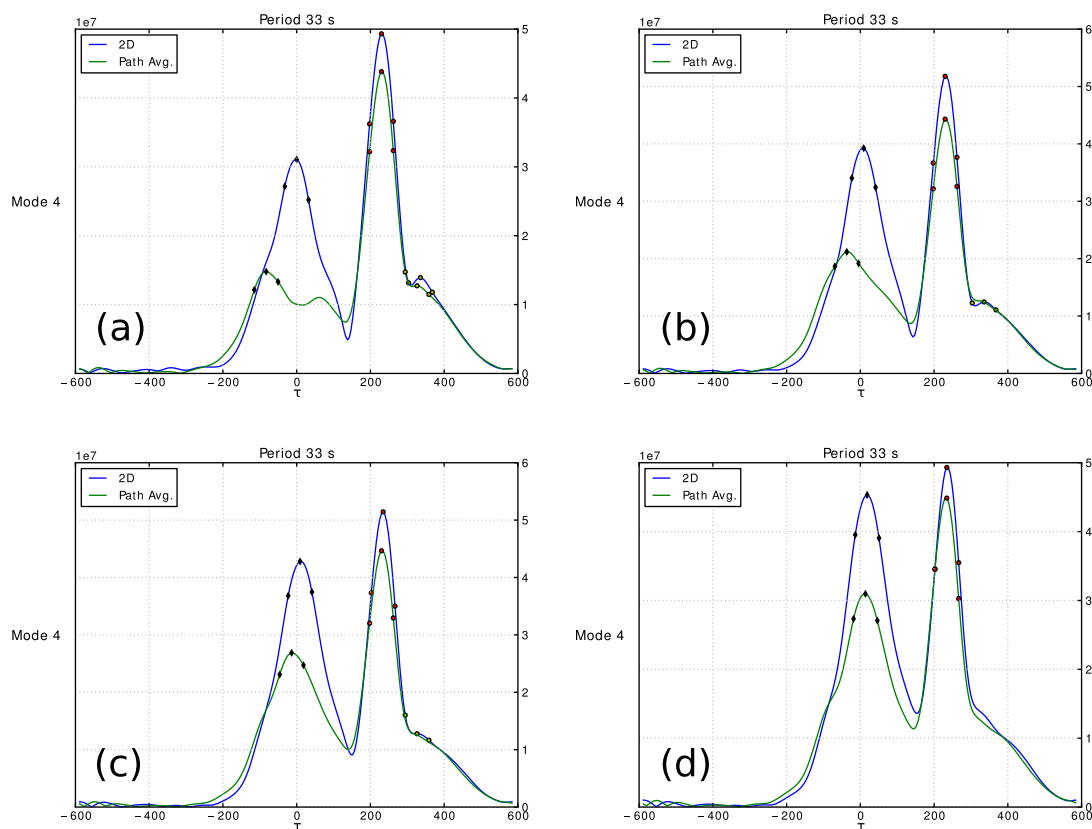
Figure 10. Mode 4 cross-correlogram at 33 s (an example correlogram chosen for illustration following Fig. 9) as a function of heterogeneity smoothness, shown for four different models: (a) P10_T0 (b) P10_T400 (c) P10_T800 (d) P10_T1200. The large phase discrepancy in the left-most lobes seen in (a) gradually disappears with increasing model smoothness. Note that for brevity in this section, the last part of the models names is dropped as all models have the same total width of heterogeneity, 2400 km.

A more general observation is related to the manner in which CL1987 processes multiple modes. For any given period, the algorithm tries to fit the fundamental mode as well as higher modes (those that are energetic enough at that period). Because the fundamental mode usually obeys the path average approximation reasonably well, it will correspond to a lobe commensurate with the true path-average model. However, the higher mode peaks (such as mode 4 in the example from Fig. 9) will deviate from the predictions of the TPA model, thereby pushing the inversion away from the true structure.

We note that this argument is similar to that of Marquering *et al.* (1996). They had a bit more clarity because they fit the fundamental mode Rayleigh wave plus the *S*-wave arrival (modelled by surface wave mode summation), and considered cases where the lateral heterogeneity is not sampled by the *S*-wave at all (it is shallow and mid path). Finally, we note that we have only attempted to understand the effect of phase (lag time) DPA. The amplitude DPA seen in this section is harder to interpret and for actual seismograms will be sensitive to attenuation (which is ignored in this study) as well as velocity structure.

5 CONCLUSIONS AND DISCUSSION

Mode conversion effects in surface wave propagation through laterally heterogeneous media have been quantified empirically. Us-ing 2-D numerical modelling, surface wave propagation has been simulated in a variety of laterally heterogeneous models and the simulation results analysed to quantitatively illuminate the nature and extent of mode conversion induced. This has been done with a bottom-up approach by studying the impact of heterogeneity on a single surface wave mode at a time. The path average approximation in ray theory-based surface wave tomography has been critically evaluated at the microscopic level, by considering individual waveform inversions.

Under the simplifying assumptions of 2-D media and normal incidence at heterogeneities (precluding off-path propagation and Love–Rayleigh coupling respectively), forward modelling in this study corroborates the theoretically expected correlation between mode conversion and heterogeneity strength and sharpness, but importantly also shows that conversion is much more significant for surface wave overtones, than for the fundamental mode. Viewed in the larger context of the twin challenges of along-path scattering (mode conversion) and off-path scattering (deviation from the GCP) in surface wave tomography, this suggests that the two said challenges are complementary; the former primarily affecting higher mode surface waves and the latter, primarily the fundamental (e.g. Ritsema *et al.* 2004).

Further, the impact of mode conversion on the CL1987 inversion technique has been demonstrated. In doing so we have looked not at the result of an inversion but at the data that actually goes into it, identifying signatures of mode coupling. No such signatures
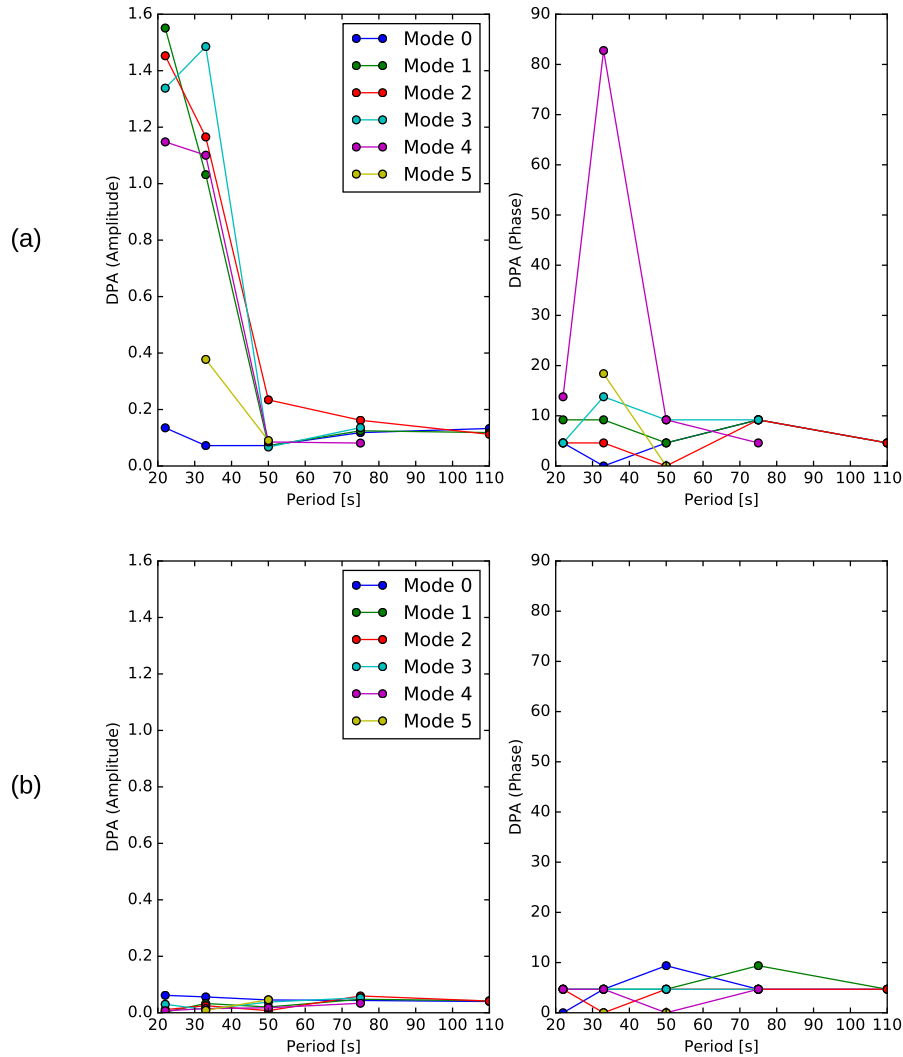
Figure 11. Quantitative measures of DPA as a function of period and mode number, shown for strong and weak heterogeneity. (a) Strong heterogeneity case: for each mode-period combination in Fig. 9, DPA is quantified as the difference between the secondary observables (specifically, the central pick of the highest-ranked[2] lobe) extracted from the 2-D data and path average data.[3] We characterize this difference by changes in amplitude (left panel) and occurrence time (right panel) of the maxima. Amplitude DPA is computed as $(\delta A/A_{\text{PAVG}})$ where $\delta A = (A_{2D} - A_{\text{PAVG}})$. Time or phase DPA is the difference in correlation lag time, $= (t_{2D} - t_{\text{PAVG}})$, δt. Note that both measures of DPA are relatively small for the fundamental mode at all periods but large for higher modes at periods less than about 50 s. At shorter periods, the effects on higher modes can be highly irregular, as evidenced by the large excursion in δt for mode 4 at 33 s. (b) Same as (a) but derived from Fig. 8(d), representing the case of weak heterogeneity with lower DPA overall.

have been found at periods of 50 s or longer, but it is clear that path-average surface wave tomography by the CL1987 method (or similar) cannot be simply extended to shorter periods (∼30 s and shorter) without revising the forward modelling on which the inversion is based. The signatures that have been found at short periods are distinct from the effects of noise in real data—noise cannot produce the kind of systematic phase perturbations seen here as a function of heterogeneity strength and sharpness. Moreover in real data inversions, noisy data are often rejected at the pre-processing stage so there is arguably a genuine cause for concern.

Although this study has focused on the effects of mode coupling on a specific inversion technique, any approach that uses a path average approximation like that in CL1987 will be similarly sensitive to the complications of mode conversions described here. The relationship between the adequacy of the path average approximation as implemented in the CL1987 approach, and the degree of lateral heterogeneity in the medium being imaged, is substantiated by forward modelling results, which are general. Within the realm of global upper mantle tomography, presuming a short period limit of 20–30 s, we infer that the effects caused by heterogeneities with strength >6 per cent and smoothness length scales <10–15λ (with a trade-off between strength and smoothness limits), will likely lie outside the realm of validity of the path average approximation. While fundamental modes may be relatively robust to these effects,

---

[2]In case of multiple lobes on the modal envelopes, the DR2012 algorithm ranks the selected lobes according to a criterion that trades off maxima amplitude against distance from reference time, as described in Debayle & Ricard (2012).

[3]For modes and periods that were not actually picked in the inversion, primarily higher modes at longer periods, candidate lobes were manually identified (where reasonable) in order to obtain sufficient data points for this figure.

they become increasingly significant in the modelling of higher modes.

REFERENCES

Aki, K. & Richards, P.G., 2002. *Quantitative Seismology,* 2nd edn, University Science Books.

Alsop, L., 1966. Transmission and reflection of Love waves at a vertical discontinuity, *J. geophys. Res.,* **71**(16), 3969–3984.

Babich, V., Chikhachev, B. & Yanovskaya, T., 1976. Surface waves in a vertically inhomogeneous elastic half-space with weak horizontal inhomogeneity, *Izv. Akad. Nauk SSSR Fiz. Zemli,* **4,** 24–31.

Baker, B. & Roecker, S., 2014. A full waveform tomography algorithm for teleseismic body and surface waves in 2.5 dimensions, *Geophys. J. Int.,* **198**(3), 1775–1794.

Bielak, J., Loukakis, K., Hisada, Y. & Yoshimura, C., 2003. Domain reduction method for three-dimensional earthquake modeling in localized regions, Part I: Theory, *Bull. seism. Soc. Am.,* **93**(2), 817–824.

Cara, M., 1978. Etude du manteau supérior à partier des harmoniques des ondes de surface, *PhD thesis,* Université Pierre er Marie Curie.

Cara, M. & Lévêque, J., 1987. Waveform inversion using secondary observables, *Geophys. Res. Lett.,* **14**(10), 1046–1049.

Debayle, E. & Kennett, B., 2000. The Australian continental upper mantle-structure and deformation inferred from surface waves, *J. geophys. Res.,* **105**(25), 423–425.

Debayle, E. & Ricard, Y., 2012. A global shear velocity model of the upper mantle from fundamental and higher Rayleigh mode measurements, *J. geophys. Res.,* **117**, B10308, doi:10.1029/2012JB009288.

Debayle, E., Kennett, B. & Priestley, K., 2005. Global azimuthal seismic anisotropy and the unique plate-motion deformation of Australia, *Nature,* **433,** 509–512.

Douma, H. & Haney, M.M., 2013. Exploring nonlinearity and nonuniqueness in surface-wave inversion for near-surface velocity estimation, *Leading Edge,* **32**(6), 648–655.

Ekström, G., Tromp, J. & Larson, E.W., 1997. Measurements and global models of surface wave propagation, *J. geophys. Res.,* **102**(B4), 8137–8157.

French, S. & Romanowicz, B., 2014. Whole-mantle radially anisotropic shear velocity structure from spectral-element waveform tomography, *Geophys. J. Int.,* **199**(3), 1303–1327.

French, S., Lekic, V. & Romanowicz, B., 2013. Waveform tomography reveals channeled flow at the base of the oceanic asthenosphere, *Science,* **342**(6155), 227–230.

Gee, L.S. & Jordan, T.H., 1992. Generalized seismological data functionals, *Geophys. J. Int.,* **111**(2), 363–390.

Gomberg, J.S. & Masters, T.G., 1988. Waveform modelling using locked-mode synthetic and differential seismograms: application to determination of the structure of Mexico, *Geophys. J. Int.,* **94**(2), 193–218.

Gregersen, S. & Alsop, L., 1974. Amplitudes of horizontally refracted Love waves, *Bull. seism. Soc. Am.,* **64**(3-1), 535–553.

Gung, Y., Panning, M. & Romanowicz, B., 2003. Global anisotropy and the thickness of continents, *Nature,* **422,** 707–711.

Heintz, M., Debaylec, E. & Vauche, A., 2005. Upper mantle structure of the South American continent and neighboring oceans from surface wave tomography, *Tectonophysics,* **406,** 115–139.

Herrera, I., 1964. On a method to obtain a Green's function for a multi-layered half space, *Bull. seism. Soc. Am.,* **54**(4), 1087–1096.

Its, E. & Yanovskaya, T., 1985. Propagation of surface waves in a half-space with vertical, inclined or curved interfaces, *Wave Motion,* **7**(1), 79–94.

Jo, C.-H., Shin, C. & Suh, J.H., 1996. An optimal 9-point, finite-difference, frequency-space, 2-D scalar wave extrapolator, *Geophysics,* **61**(2), 529–537.

Kennett, B., 1984. Guided wave propagation in laterally varying media–I. Theoretical development, *Geophys. J. Int.,* **79**(1), 235–255.

Kennett, B., 1998. Guided waves in three-dimensional structures, *Geophys. J. Int.,* **133**(1), 159–174.

Lay, T. & Kanamori, H., 1985. Geometric effects of global lateral heterogeneity on long-period surface wave propagation, *J. geophys. Res.,* **90**(B1), 605–621.

Lekić, V. & Romanowicz, B., 2011. Inferring upper-mantle structure by full waveform tomography with the spectral element method, *Geophys. J. Int.,* **185**(2), 799–831.

Levshin, A.L., Barmin, M.P., Ritzwoller, M.H. & Trampert, J., 2005. Minor-arc and major-arc global surface wave diffraction tomography, *Phys. Earth planet. Inter.,* **149**(3), 205–223.

Li, X.-D. & Romanowicz, B., 1995. Comparison of global waveform inversions with and without considering cross-branch modal coupling, *Geophys. J. Int.,* **121**(3), 695–709.

Li, X.-D. & Romanowicz, B., 1996. Global mantle shear velocity model developed using nonlinear asymptotic coupling theory, *J. geophys. Res.,* **101**(B10), 22 245–22 272.

Li, X.-D. & Tanimoto, T., 1993. Waveforms of long-period body waves in a slightly aspherical earth model, *Geophys. J. Int.,* **112**(1), 92–102.

Maggi, A., Debayle, E., Priestley, K. & Barruol, G., 2006. Multimode surface waveform tomography of the Pacific Ocean: a closer look at the lithospheric cooling signature, *Geophys. J. Int.,* **166,** 1384–1397.

Marquering, H. & Snieder, R., 1995. Surface-wave mode coupling for efficient forward modelling and inversion of body-wave phases, *Geophys. J. Int.,* **120**(1), 186–208.

Marquering, H. & Snieder, R., 1996. Shear-wave velocity structure beneath Europe, the northeastern Atlantic and western Asia from waveform inversions including surface-wave mode coupling, *Geophys. J. Int.,* **127**(2), 283–304.

Marquering, H., Snieder, R. & Nolet, G., 1996. Waveform inversions and the significance of surface-wave mode coupling, *Geophys. J. Int.,* **124**(1), 258–278.

Maupin, V., 2007. Introduction to mode coupling methods for surface waves, *Adv. Geophys.,* **48,** 127–155.

Mégnin, C. & Romanowicz, B., 2000. The three-dimensional shear velocity structure of the mantle from the inversion of body, surface and higher-mode waveforms, *Geophys. J. Int.,* **143**(3), 709–728.

Meier, T., Lebedev, S., Nolet, G. & Dahlen, F., 1997. Diffraction tomography using multimode surface waves, *J. geophys. Res.,* **102**, 8255–8267.

Mendiguren, J.A., 1977. Inversion of surface wave data in source mechanism studies, *J. Geophys. Res.,* **82**(5), 889–894.

Montelli, R., Nolet, G., Dahlen, F., Masters, G., Engdahl, E.R. & Hung, S.-H., 2004. Finite-frequency tomography reveals a variety of plumes in the mantle, *Science,* **303**(5656), 338–343.

Moulik, P. & Ekström, G., 2014. An anisotropic shear velocity model of the Earth's mantle using normal modes, body waves, surface waves and long-period waveforms, *Geophys. J. Int.,* **199**(3), 1713–1738.

Nettles, M. & Dziewoński, A.M., 2008. Radially anisotropic shear velocity structure of the upper mantle globally and beneath North America, *J. geophys. Res.,* **113,** B02303, doi:10.1029/2006JB004819.

Nolet, G., 1990. Partitioned waveform inversion and two-dimensional structure under the Network of Autonomously Recording Seismographs, *J. geophys. Res.,* **95,** 8499–8512.

Panning, M. & Romanowicz, B., 2006. A three-dimensional radially anisotropic model of shear velocity in the whole mantle, *Geophys. J. Int.,* **167**(1), 361–379.

Park, C.B., Miller, R.D. & Xia, J., 1998. Imaging dispersion curves of surface waves on multi-channel record, in *SEG Expanded Abstracts,* vol. 17, pp. 1377–1380.

Peterson, J., 1993. Observations and modeling of seismic background noise, *U.S. Geological Survey Open-File Report 93–322*, U.S. Geological Survey, Albuquerque, New Mexico.

Pollitz, F.F., 1994. Global tomography from rayleigh and love wave dispersion: effect of ray-path bending, *Geophys. J. Int.,* **118**(3), 730–758.

Priestley, K. & Debayle, E., 2003. Seismic evidence for a moderately thick lithosphere beneath the Siberian Platform, *Geophys. Res. Lett.,* **30**(3), 1118, doi:10.1029/2002GL015931.

Priestley, K. & McKenzie, D., 2006. The thermal structure of the lithosphere from shear wave velocities, *Earth planet. Sci. Lett.,* **244**, 285–301.

Priestley, K. & McKenzie, D., 2013. The relationship between shear wave velocity, temperature, attenuation and viscosity in the shallow part of the mantle, *Earth planet. Sci. Lett.,* **381**, 78–91.

Priestley, K., Debayle, E., McKenzie, D. & Pilidou, S., 2006. Upper mantle structure of eastern Asia from multimode surface waveform tomography, *J. geophys. Res.,* **111**, B10304, doi:10.1029/2005JB004082.

Priestley, K., McKenzie, D., Debayle, E. & Pilidou, S., 2008. The African upper mantle and its relationship to tectonics and surface geology, *Geophys. J. Int.,* **175**(3), 1108–1126.

Ritsema, J., van Heijst, H.J. & Woodhouse, J.H., 2004. Global transition zone tomography, *J. geophys. Res.,* **109**, B02302, doi:10.1029/2003JB002610.

Ritzwoller, M.H., Shapiro, N.M., Barmin, M.P. & Levshin, A.L., 2002. Global surface wave diffraction tomography, *J. geophys. Res.,* **107**(B12), 2335, doi:10.1029/2002JB001777.

Roecker, S., Baker, B. & McLaughlin, J., 2010. A finite-difference algorithm for full waveform teleseismic tomography, *Geophys. J. Int.,* **181**(2), 1017–1040.

Schaeffer, A. & Lebedev, S., 2013. Global shear speed structure of the upper mantle and transition zone, *Geophys. J. Int.,* **194**, 417–449.

Sieminski, A., Lévêque, J. & Debayle, E., 2004. Can finite-frequency effects be accounted for in ray theory surface wave tomography?, *Geophy. Res. Lett.,* **31**, L24614, doi:10.1029/2004GL021402.

Štekl, I. & Pratt, R.G., 1998. Accurate viscoelastic modeling by frequency-domain finite differences using rotated operators, *Geophysics,* **63**(5), 1779–1794.

Szelwis, R., 1983. A hybrid approach to mode conversion, *Geophys. J. Int.,* **74**(3), 887–904.

Takeuchi, H. & Saito, M., 1972. Seismic surface waves, in *Methods in Computational Physics,* vol. 11, pp. 217–295, ed. Bolt, B., Academic Press.

Thatcher, W. & Brune, J.N., 1969. Higher mode interference and observed anomalous apparent Love wave phase velocities, *J. geophys. Res.,* **74**(27), 6603–6611.

Trampert, J. & Spetzler, J., 2006. Surface wave tomography: finite-frequency effects lost in the null space, *Geophys. J. Int.,* **164**(2), 394–400.

Trampert, J. & Woodhouse, J., 1995. Global phase velocity maps of Love and Rayleigh waves between 40 and 150 seconds, *Geophys. J. Int.,* **22**, 675–690.

Tromp, J., 1994. A coupled local-mode analysis of surface-wave propagation in a laterally heterogeneous waveguide, *Geophys. J. Int.,* **117**(1), 153–161.

Tromp, J. & Dahlen, F., 1992a. Variational principles for surface wave propagation on a laterally heterogeneous Earth—I. Time-domain JWKB theory, *Geophys. J. Int.,* **109**(3), 581–598.

Tromp, J. & Dahlen, F., 1992b. Variational principles for surface wave propagation on a laterally heterogeneous Earth—II. Frequency-domain JWKB theory, *Geophys. J. Int.,* **109**(3), 599–619.

Van Der Hilst, R.D. & De Hoop, M.V., 2005. Banana-doughnut kernels and mantle tomography, *Geophys. J. Int.,* **163**(3), 956–961.

Van der Kruk, J., Arcone, S. & Liu, L., 2007. Fundamental and higher mode inversion of dispersed GPR waves propagating in an ice layer, *IEEE Trans. Geosci. Remote Sens.,* **45**(8), 2483–2491.

van Heijst, H. & Woodhouse, J., 1997. Measuring surface-wave overtone phase velocities using a mode-branch stripping technique, *Geophys. J. Int.,* **131**, 209–230.

Wang, Z., Tromp, J. & Ekström, G., 1998. Global and regional surface-wave inversions: a spherical-spline parameterization, *Geophys. Res. Lett.,* **25**(2), 207–210.

Woodhouse, J., 1974. Surface waves in a laterally varying layered structure, *Geophys. J. R. astr. Soc.,* **37**, 461–490.

Woodhouse, J.H. & Dziewonski, A.M., 1984. Mapping the upper mantle: three-dimensional modeling of Earth structure by inversion of seismic waveforms, *J. geophys. Res.,* **89**, 5953–5986.

Woodhouse, J.H. & Wong, Y.K., 1986. Amplitude, phase and path anomalies of mantle waves, *Geophys. J. Int.,* **87**(3), 753–773.

Yomogida, K., 1985. Gaussian beams for surface waves in laterally slowly-varying media, *Geophys. J. Int.,* **82**(3), 511–533.

Zhao, L. & Jordan, T.H., 1998. Sensitivity of frequency-dependent travel-times to laterally heterogeneous, anisotropic earth structure, *Geophys. J. Int.,* **133**(3), 683–704.

Zhou, Y., Dahlen, F. & Nolet, G., 2004. Three-dimensional sensitivity kernels for surface wave observables, *Geophys. J. Int.,* **158**(1), 142–168.

APPENDIX A: FINITE DIFFERENCE TESTING

On using the FD solver to model surface wave propagation to large distances (tens of wavelengths), it was found that the results were sensitive to the level of discretization, that is, grid density, used in the modelling. This suggests that the code suffers from numerical dispersion effects—a common problem with FD methods used to solve wave equations. At short distances the effects are negligible but since the purpose of this study is to compute synthetic seismograms at distances typical in global/regional surface wave tomography, extensive code testing was carried out to ensure reliable results.

Tests were performed with the model of Fig. A1, chosen for its simplicity as it is derived from the simplest type of model that can allow dispersive surface waves—a layer over a half-space. This model is also well suited to testing different grid densities because everything about its geometry ensures equivalent discretization by an 8, 6, 4 or 3 km grid—the regular and perturbed layer thicknesses are 48 and 24 km respectively, the perturbation in layer thickness starts at 120 km and is 192 km wide. Setting a high frequency limit of 0.08 Hz (12.5 s period) for the modelling, velocities in the model were chosen such that the shortest Rayleigh wavelength is 48 km. The values 8, 6, 4 and 3 km for the grid spacing correspond to 6, 8, 12 and 16 grid points per shortest wavelength (GPPSW), respectively. Testing was done with an earthquake source 1000 km outside the model (on the left side) and at a depth of 72 km depth, which ensured good Rayleigh wave fundamental mode excitation up to 0.08 Hz.

Fig. A2 compares the results of the test obtained with different grid sizes. It is clear that the short wavelengths (late arrivals) are more strongly affected by the grid spacing than the long wavelengths, and that the problem worsens with distance. At large distances (∼100 times the shortest wavelength) a grid spacing of 12 GPPSW is required for robust computations.

A1 Testing

We test the FD output against known theoretical results for simple models of lateral heterogeneity which consist of a single, plane
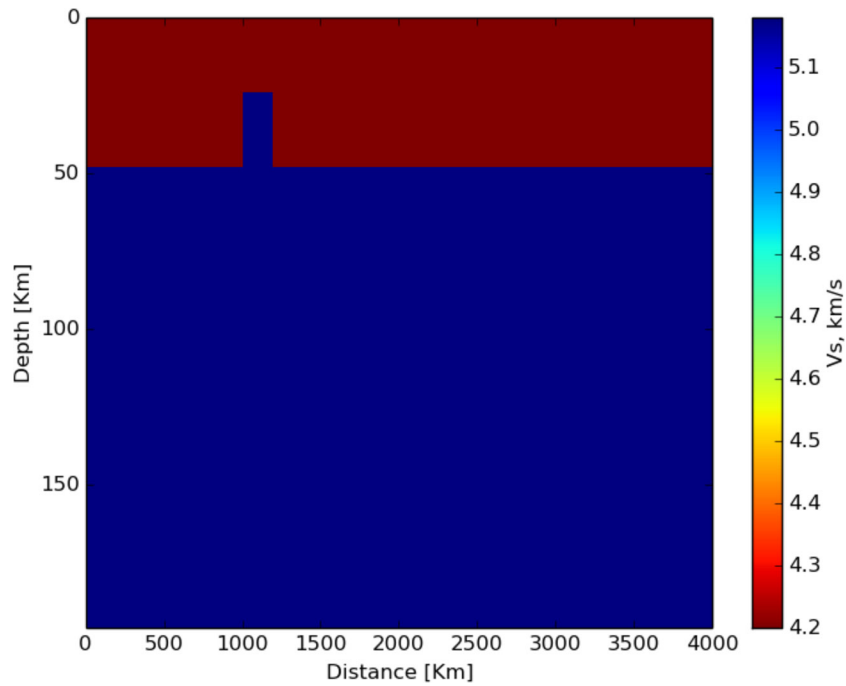
Figure A1. Grid-test model used for the tests shown in Fig. A2. It is derived by perturbing (with a local change in layer thickness) a 1-D layer over half-space model.
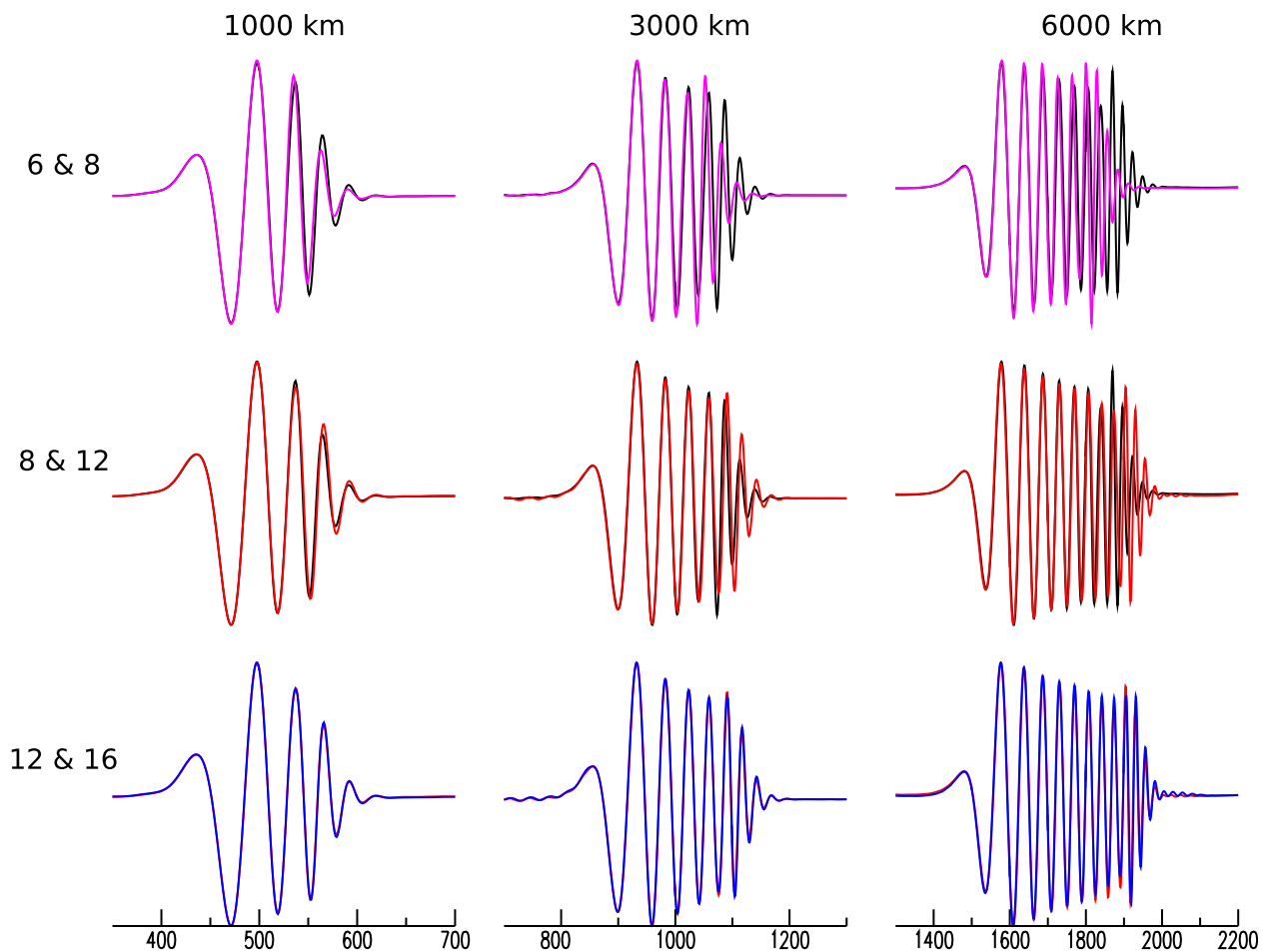

Figure A2. Vertical component synthetic seismograms at three different distances for Rayleigh wave propagation in the grid-test model, shown as a pairwise comparison of the result with 6 (magenta), 8 (black), 12 (red) and 16 (blue) GPPSW as indicated on the left-hand side. Note that distances indicated are in the model, not epicentral distances, as the source is outside the model.

vertical contact between two laterally homogeneous regions. Models of this type have been extensively studied in the seismological literature, using a variety of semi-analytical techniques that express the wavefield in terms of incident, reflected and transmitted waves, thereby reducing the problem to the evaluation of reflection and transmission coefficients.

All test models are derivatives of the layer-over-half-space type and we use four different models as shown in Fig. A3—(a) a single layer, single step model with no change in elastic parameters; (b) a similar model with change in parameters; (c) a multilayer single step model with change; (d) a double step model with no change in parameters. For each of these models, the Love and Rayleigh fundamental mode reflection/transmission problem is (separately) solved in this study—using the same analytical method as the original publication from which the model is taken in case of Love waves, and using the Green's function method of Its & Yanovskaya (1985) for Rayleigh waves, regardless of model. The observable/quantity used for benchmarking is the ratio of surface displacement in the transmitted field to that in the incident field, hereafter called the *transmission surface ratio*. In case of FD modelling results, this quantity is measured by dividing the MPFs of the transmitted field by those of the incident field, which in all cases consists of just the fundamental mode. Having confirmed that the analytical results obtained in this study match those in the published literature, we compare the FD modelling result for each model with the corresponding analytical result, in Fig. A4. Implementation of the analytical techniques in this study, rather than simply comparing with published results, allows deviations (such as may be required by the FD grid) from or extensions to the exact model type, frequencies and mode numbers for which published results are available. For example, the Love wave result in Fig. A4(c) shows conversion to multiple higher modes—the ability to make such a measurement is critical to this paper but higher mode results for this model are not available in the published literature even though this model has been independently used in multiple studies.

Based entirely on visual inspection, agreement with theory is deemed to be acceptable in all cases. Following Section 2.2.2 we also compute energy transmission coefficients and find that FD modelling results differ from the analytical ones by up to 20 per cent. However it must be borne in mind that the analytical results are not exact—the techniques are approximate in principle and subject to numerical integration errors in practice.
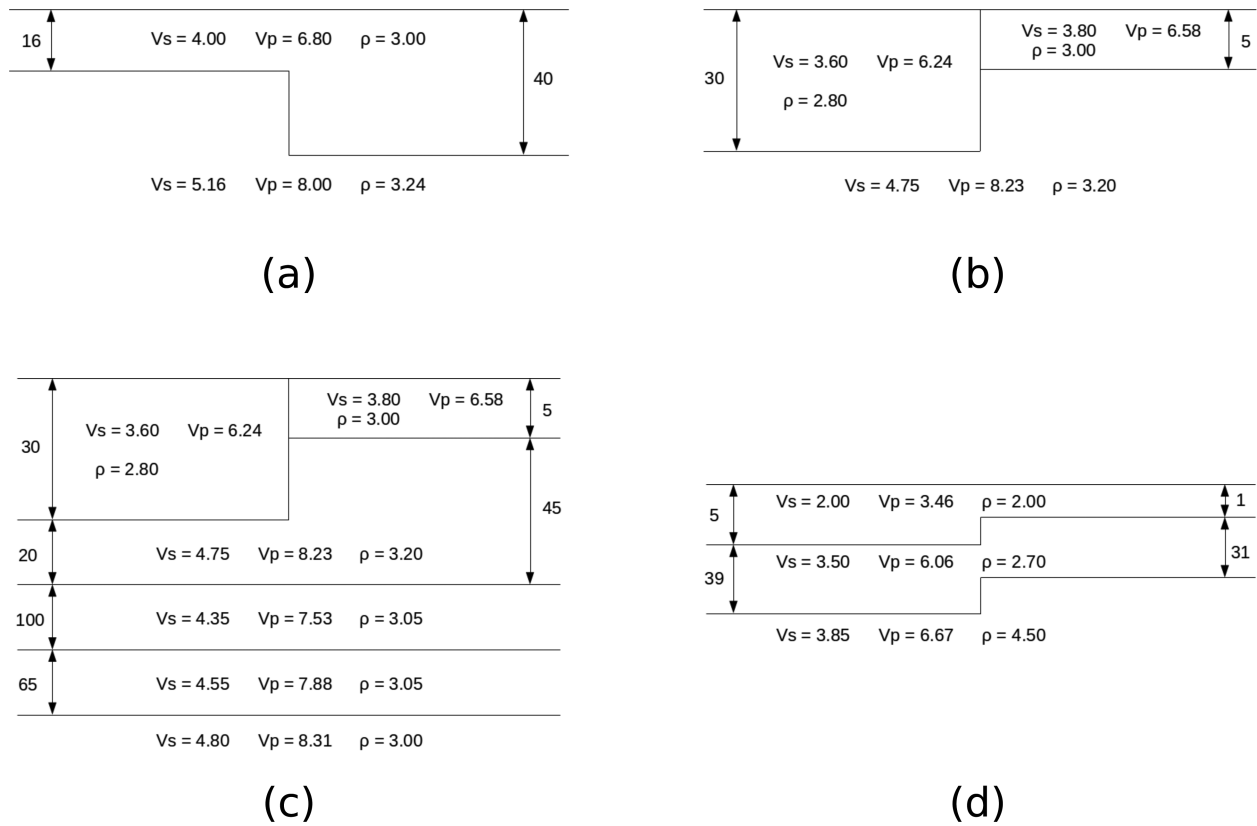

Figure A3. Schematic representation of models used for testing of FD calculations against analytical results: (a) M-discontinuity model of Alsop (1966), shown with the V_p values (unspecified in original model) used in this study. (b,c) Models F and L respectively, from Gregersen & Alsop (1974); modified slightly from original in that the crustal thickness on the RHS is taken as 5 km rather than 7 km, to facilitate use of a 2.5 km FD grid. (d) Double-step model from Its & Yanovskaya (1985). In all cases layer thicknesses are shown in km and units for velocity and density are km s^{-1} and gm cc^{-1}, respectively.
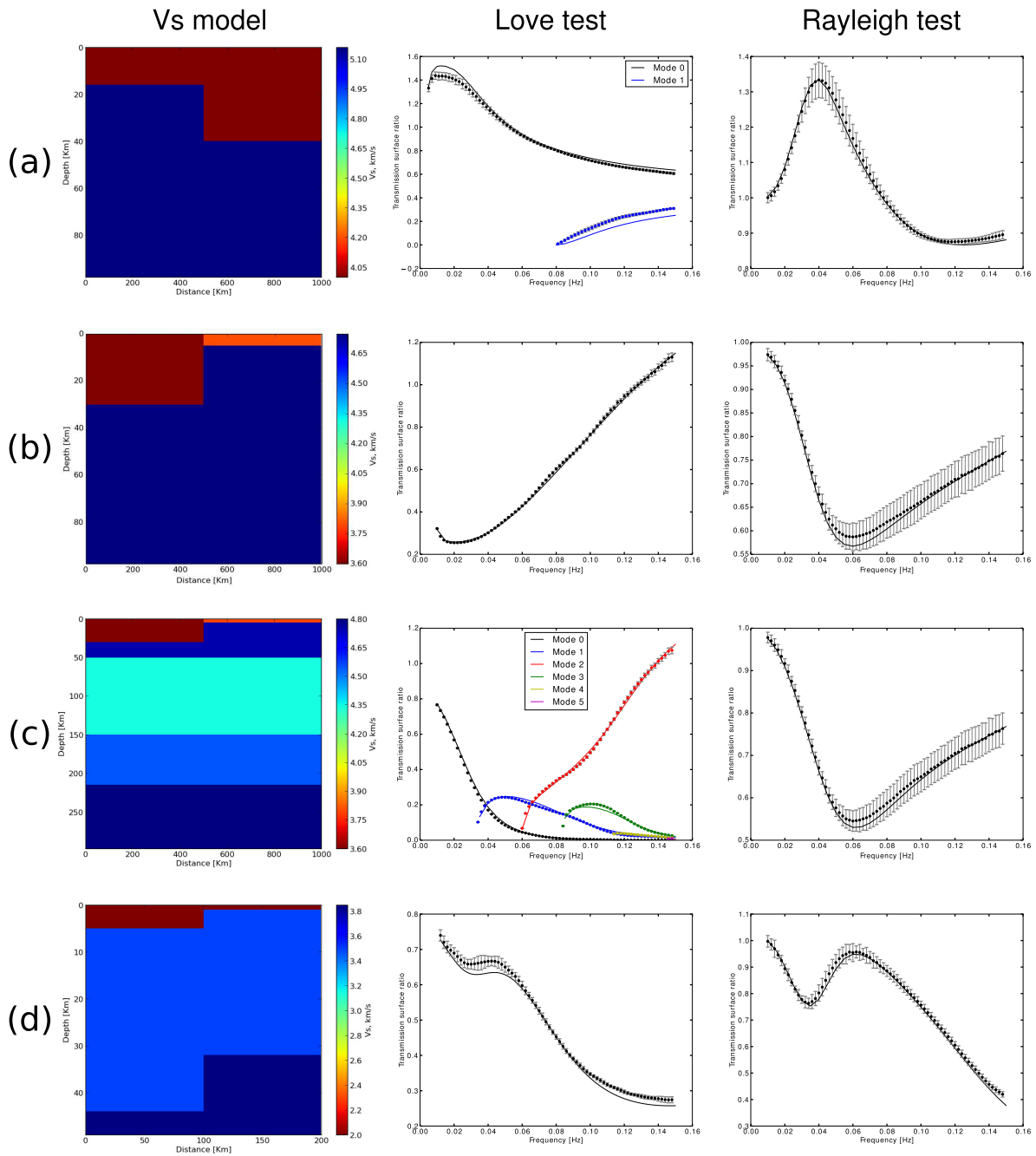
Figure A4. Test results for the same models (a)–(d) as Fig. A3. The left column shows the V_s structure for these models as implemented on the FD grid, middle and right columns show the results for Love and Rayleigh wave tests respectively. In each case a fundamental mode wave propagates from left to right in the model and results are visualized in terms of the transmission surface ratio plotted as a function of frequency. Solid lines show the analytic results obtained in this study and the dots with error bars show the results from FD modelling. The incident fundamental mode is shown in black and, where applicable, higher modes are shown with the colours indicated on individual plot legends. Note that conversion to higher modes is not considered in the Rayleigh wave tests.

APPENDIX B: WAVEFIELD FITTING ERRORS

The mode-wise amplitude spectrum (surface displacement amplitude) of the earthquake source used in this study is shown in Fig. B1.

The corresponding spurious mode measurements (modes other than input mode measured by the wavefield fitting method when the model is 1-D and the input is a single mode) in the background model used in this study are shown in Figs B2 and B3 for Love and Rayleigh modes, respectively.
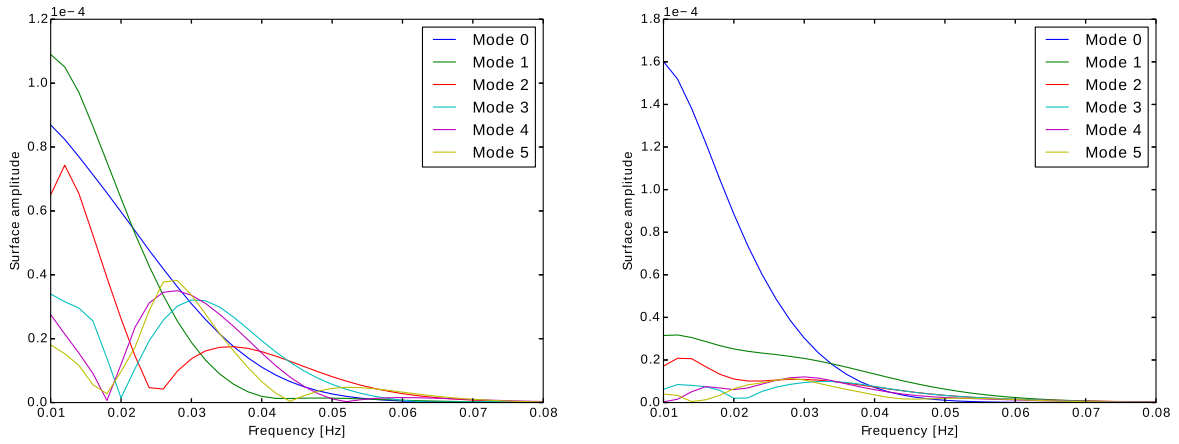

Figure B1. Mode amplitudes in the transverse (left) and vertical (right) component of displacement due to the chosen source, in the chosen background model, reflecting the source excitation of Love and Rayleigh wave modes respectively. In the Rayleigh wave case the fundamental mode dominates at low frequencies but there is still good excitation of the overtones.
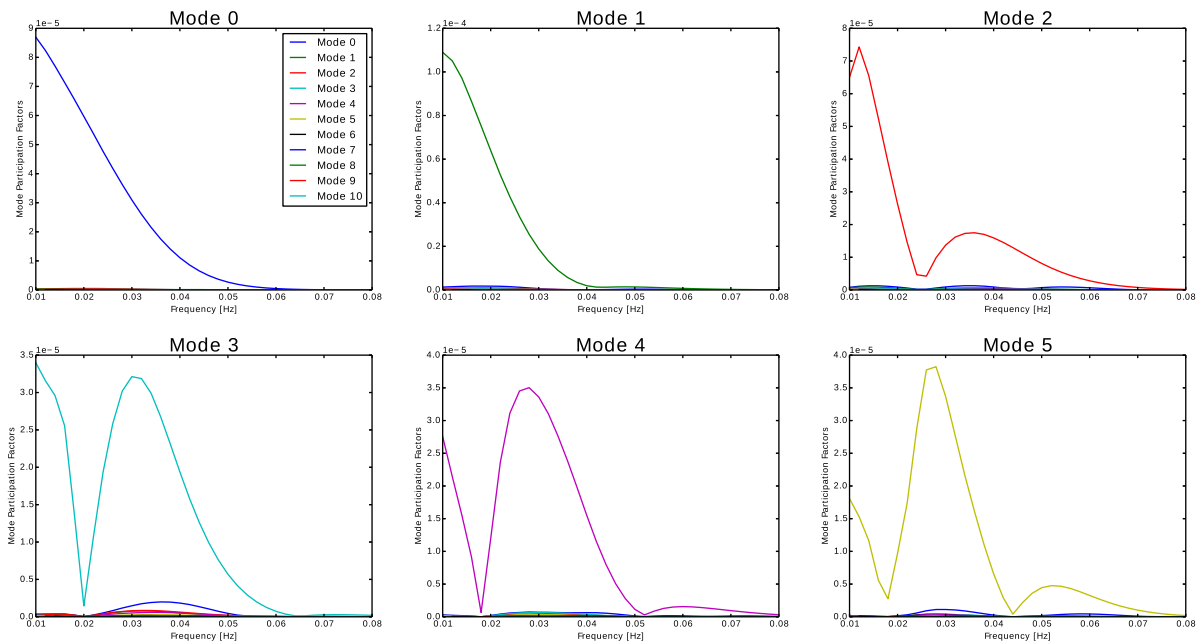

Figure B2. Measurement of individual Love wave modes (a_i values) which are separately input to the $1-$D background model (mode number indicated above each plot), showing the amplitude of spurious modes measured. Note the correspondence of the genuine mode measurement with Fig. B1, left panel. In case of the overtones, the spurious modes are dominated by the fundamental mode, as is most clearly visible for the third overtone.
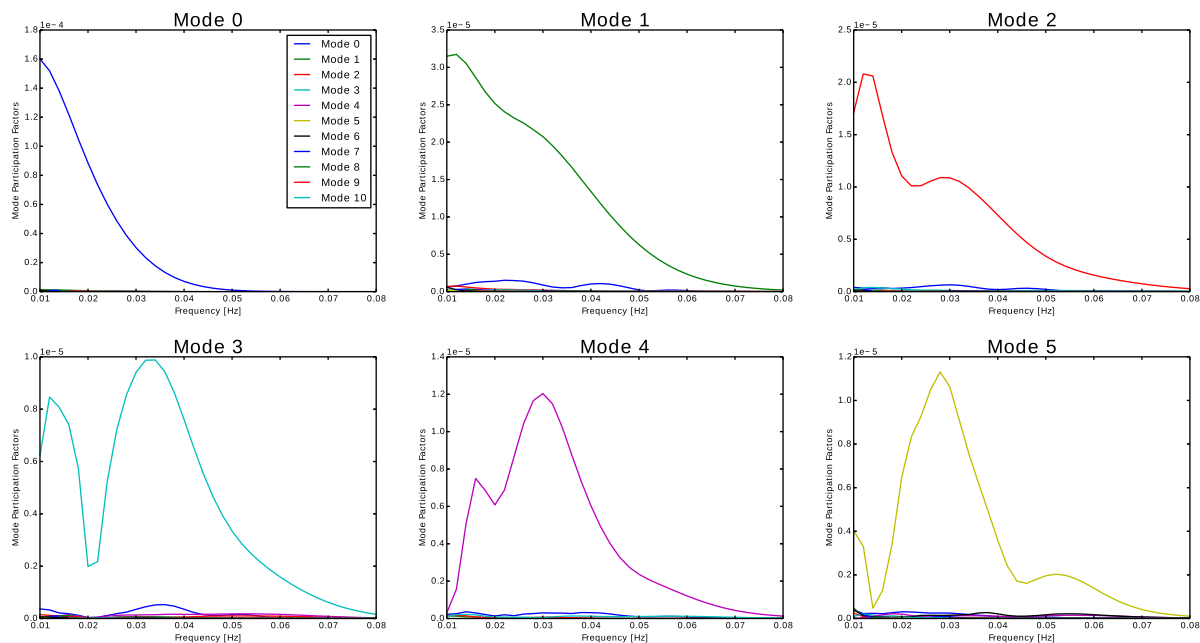
Figure B3. Same as Fig. B2 but for Rayleigh modes. Genuine mode measurements correspond to the right panel of Fig. B1.

SUPPORTING INFORMATION

Supplementary data are available at *GJI* online.

APPENDIX C

Figure C1. Love (top) and Rayleigh (bottom) wave mode-wise results for model P10_T0_W1200 (the canonical study model).

Figure C2. Love (top) and Rayleigh (bottom) wave mode-wise results for model P8_T0_W1200.

Figure C3. Love (top) and Rayleigh (bottom) wave mode-wise results for model P6_T0_W1200.

Figure C4. Love (top) and Rayleigh (bottom) wave mode-wise results for model P4_T0_W1200.

Figure C5. Love (top) and Rayleigh (bottom) wave mode-wise results for model_P2_T0 W1200.

Figure C6. Love (top) and Rayleigh (bottom) wave mode-wise results for model P10_T0_W2400.

Figure C7. Love (top) and Rayleigh (bottom) wave mode-wise results for model P10_T400_W2400.

Figure C8. Love (top) and Rayleigh (bottom) wave mode-wise results for model P10_T800_W2400.

Figure C9. Love (top) and Rayleigh (bottom) wave mode-wise results for model P10_T1200_W2400.

Figure C10. Love (top) and Rayleigh (bottom) wave mode-wise results for model N10_T0_W3200. Reciprocity between modes 0–1

is clearly visible in the Love wave case. Note that these are energy plots and the fundamental mode having nearly the same energy as the incident first overtone (at ∼0.065 Hz) implies it has an amplitude significantly larger (4–5 times) than that of the incident mode.

Figure C11. Love (top) and Rayleigh (bottom) wave mode-wise results for model N10_T400_W3200.

Figure C12. Love (top) and Rayleigh (bottom) wave mode-wise results for model N10_T800_W3200.

Figure C13. Love (top) and Rayleigh (bottom) wave mode-wise results for model N10_T1200_W3200.

Figure C14. Love (top) and Rayleigh (bottom) wave mode-wise results for model N10_T1600_W3200.

Figure C15. Love wave mode conversion as a function of strength of heterogeneity. Models included: P2_T0, P4_T0, P6_T0, P8_T0 and P10_T0. Format is same as that of Fig. 6 in main text.

Figure C16. Love wave mode conversion as a function of strength of heterogeneity. Models included: P2_T0, P4_T0, P6_T0, P8_T0 and P10_T0. Format is same as that of Fig. 6 in main text.

Figure C17. Mode 4 cross-correlogram at 33 s as a function of heterogeneity strength, shown for four different models: (a) P8_T0 (b) P6_T0 (c) P4_T0 (d) P2_T0. Similar to Fig. 10 of main text, with the P10 T0 case shown therein.

Please note: Oxford University Press is not responsible for the content or functionality of any supporting materials supplied by the authors. Any queries (other than missing material) should be directed to the corresponding author for the paper.